



# 1 **Effects of dynamic changes of desiccation cracks on preferential flow: Experimental investigation and** 2 **numerical modeling**

3

4 Yi Luo<sup>1,2</sup>, Jiaming Zhang\*<sup>1</sup>, Zhi Zhou<sup>3</sup>, Juan P. Aguilar-Lopez<sup>4</sup>, Roberto Greco<sup>5</sup>, Thom Bogaard<sup>2</sup>

5 <sup>1</sup> Faculty of Engineering, China University of Geosciences (Wuhan), Wuhan, 430074, China

6 <sup>2</sup> Water Resources Section, Faculty of Civil Engineering and Geosciences, Delft University of Technology, Stevinweg 1, P.O.  
7 Box 5048, 2600 GA Delft, the Netherlands

8 <sup>3</sup> Department of Engineering Management, Hubei University of Economics, Wuhan, 430205, China

9 <sup>4</sup> Department of Hydraulic Engineering, Faculty of Civil Engineering and Geosciences, Delft University of Technology, Delft,  
10 2600 GA, the Netherlands

11 <sup>5</sup> Dipartimento di Ingegneria, Università degli Studi della Campania “Luigi Vanvitelli”, via Roma 29, 81031, Aversa, Italy

12 *Correspondence to:* Jiaming Zhang ([zjm@cug.edu.cn](mailto:zjm@cug.edu.cn))

13

14 **Abstract:** Preferential flow induced by desiccation cracks (PF-DC) has been proven to be an important hydrological effect  
15 that could cause various geotechnical engineering and ecological environment problems. Investigation on the PF-DC remains  
16 a great challenge due to the soil shrinking-swelling behavior. This work presents an experimental and numerical study of the  
17 PF-DC considering the dynamic changes of DC. A soil column test was conducted under wetting-drying cycles to investigate  
18 the dynamic changes of DC and their hydrological response. The ratio between the crack area and soil matrix area (crack  
19 ratio), crack aperture and depth were measured. The soil water content, matrix suction and water drainage were monitored. A  
20 new dynamic dual-permeability preferential flow model (DPMDy) was developed, which includes physically-consistent  
21 functions in describing the variation of both porosity and hydraulic conductivity in crack and matrix domains. Its performance  
22 was compared to the single-domain model (SDM) and rigid dual-permeability model (DPM) with fixed crack ratio and  
23 hydraulic conductivity. The experimental results showed that the maximum crack ratio and aperture decreased when the  
24 evaporation intensity was excessively raised. The self-closure phenomenon of cracks and increased surficial water content  
25 were observed during low evaporation periods. The simulation results showed that the matrix evaporation modeled by the  
26 DPMDy is lower than that of the SDM and DPM, but its crack evaporation is the highest. Compared to the DPM, the DPMDy  
27 simulated a faster pressure head building-up process in the crack domain and higher water exchange rates from the crack to  
28 the matrix domain during rainfall. Using a fixed crack ratio in the DPM, whether it is the maximum or the average value from  
29 the experiment data, will overestimate the infiltration fluxes of PF-DC but underestimate its contribution to the matrix domain.  
30 In conclusion, the DPMDy better described the underlying physics involving crack evolution and hydrological response with  
31 respect to the SDM and DPM. Further improvement of the DPMDy should focus on the hysteresis effect of the SWRC curve  
32 and soil deformation during wetting-drying cycles.

33 **Keywords:** Desiccation cracks; preferential flow; dynamic changes; dual-permeability model; wetting-drying cycles

## 34 **1. Introduction**

35 Desiccation cracks are prevalent in clay-dominated soils due to water loss, which often lead water to bypass the surface soil  
36 matrix and rapidly infiltrate into subsoil as preferential flow (Davidson, 1984; Weiler, 2005). Positively, the preferential flow  
37 induced by desiccation cracks (PF-DC) can promote the migration of farmland organic matter (Vervoort et al., 2003) and  
38 reduce surface runoff (Pei et al., 2020; Zhang et al., 2021a). Negatively, it also has proven to be an important hydrological



39 mechanism that could lead to geotechnical engineering and ecological environment problems, such as dike and slope  
40 instability (Jamalinia et al., 2020; Zhang et al., 2021b), shallow landslides (Bogaard and Greco, 2015; Caris and Van Asch,  
41 1991; Luo et al., 2021), groundwater pollution (Chaduvula et al., 2022; Chen et al., 2002; Mooney and Morris, 2008; Schlögl  
42 et al., 2022) and reduction of irrigation efficiency (Greve et al., 2010; Smith et al., 2005; Wang et al., 2018; Wang et al., 2022).  
43 Under the current background of frequent extreme flood-drought climate events, its negative effects will be more prominent  
44 (Tichavsky et al., 2019). Investigation on the PF-DC are of great significance in guiding scientific research and practical  
45 design in the above disciplines.

46 A unique characteristic of the desiccation cracks is their dynamic features, often causing instantaneous variation of crack  
47 proportion, depth and connectivity with moisture content. Previous efforts have attempted to reveal the effects of crack  
48 dynamics on the PF-DC through experiment studies, but most of them focused on short-term wetting process and obtained  
49 only qualitative results and debates remained. For instance, Favre et al. (1997) and Liu et al. (2003) stated that crack closure  
50 due to wetting can cause a significant reduction or even disappearances in the preferential flow. However, other studies found  
51 that the PF-DC also leads water to rapidly infiltrate into deep soil even desiccation cracks are nearly closed (Baram et al.,  
52 2012a; Greve et al., 2010; Luo et al., 2021; Tuong et al., 1996; Sander and Gerke, 2007). Cheng et al. (2021) conducted a  
53 series of constant-head permeability tests with the hydraulic head gradient of 15 kPa. They stated that 4% of surface crack  
54 ratio could be a critical value for determining whether desiccation cracks cause a significant increase in the infiltration rate or  
55 not. However, this value may vary with different soils, rainfall patterns and sample scales, and thus lacks general applicability.  
56 Indeed, PF-DC has long-term and complex spatiotemporal variability due to crack dynamics during wetting-drying cycles.  
57 Therefore, short-term and small-scale infiltration tests (i.e. laboratory permeability tests) are not enough to reveal the complex  
58 hydrological process induced by PF-DC. Meanwhile, it is also difficult to quantitatively study PF-DC only through  
59 experiments. An improve understanding of the PF-DC combined with theory methods is also needed.

60 Regarding the theoretical methods, explicit crack models (EMs) (Hendrickx. and Flury, 2001; Khan et al., 2017; Xie et al.,  
61 2020)), dual-porosity (DPoM) (Van Genuchten, 1980; Van Genuchten and Wierenga, 1976) and dual-permeability (DPM)  
62 (Aguilar - López et al., 2020; Gerke and Van Genuchten, 1993b, 1993a) models were developed to simulate preferential flow  
63 in cracked clay soils. EMs were constructed based on the single-domain (or single-permeability) framework, which require  
64 to define the details involving the geometry, spatial distribution and hydrological properties of each crack. Such requirement  
65 may be conceptually correct but makes them difficult for simulating network-distributed desiccation cracks due to  
66 considerable computational burden (Aguilar - López et al., 2020). The DPoM and DPM concepts belong to the dual-domain  
67 framework that assumes the soil pore system can be represented as two overlapping interacting regions, one which represents  
68 the matrix domain with micropores and the other one represents the crack domain with meso-macro pores (Šimůnek et al.,  
69 2003). Those models represent the cracks in the soil as implicit form which need not to prescribe geometrical and spatial  
70 features of the desiccation cracks. The DPoM concept holds the simplifying stipulation that water only flows through the  
71 shrinkage cracks rather than the soil matrix, which is unrealistic in many cases. To remedy this shortcoming, classical DPM  
72 was developed, where, the water flow in soil matrix and crack domain was simulated using the Richards' equation (Aguilar -  
73 López et al., 2020; Coppola et al., 2012; Gerke and Maximilian Köhne, 2004; Gerke and Van Genuchten, 1993a) or Green-  
74 Ampt model (Davidson, 1984; Stewart, 2019; Weiler, 2005) building on Darcy's law. However, some critics emerged that  
75 the Richards' equation building on the capillarity, not existing in large PF paths (e.g. tensile cracks and biological holes), is  
76 not suitable to simulate the PF (Larsbo and Jarvis, 2003; Nimmo, 2010; 2021). Consequently, some improved DPMs were  
77 developed, where, water flow in the crack domain was simulated by the Navier-Stokes equation (Germann and Karlen, 2016;  
78 Nimmo, 2010), kinematic wave equation (Greco, 2002; Larsbo and Jarvis, 2003) and Poiseuille model (Lepore et al., 2009).  
79 Although these improved DPM models better captured the characteristics of the water flow in the crack domain, the classical  
80 DPM concept has still been widely accepted and used in simulating preferential flow in soils due to its easily available



81 parameters, reasonably satisfactory prediction to the measurements and high computation efficiency (Jarvis et al., 2016). Most  
82 importantly, a recent numerical study conducted by Aguilar - López et al. (2020) proved that effective parameter selection in  
83 the DPM models can achieve similar modeling results to the EMs.  
84 Nevertheless, classical DPM models often adopt the assumption that crack volume and hydrological properties keep constant  
85 in both time and space, which is unfeasible to capture the full dynamics of PF-DC. Some attempts have been made to  
86 incorporate the dynamic nature of desiccation cracks into DPM including the SWAP family of models, i.e. LEACHM, which  
87 simulates PF-DC using a shrinkage characteristic and water loss (Kroes et al., 2000), but neglects water exchange process  
88 occurring at the interface between two domains. Such a process has widely been confirmed to be significant in cracked soils  
89 (Greve et al., 2010; Krisnanto et al., 2016; Tuong et al., 1996). Later modification of SWAP incorporated the aforementioned  
90 process, but with a cost of neglecting shrink-swell behavior of soil. The VIMAC model developed by Greco (2002) solved  
91 previous problems but against the cost of inducing many parameters which are difficult to determine from experiments or  
92 measurements. Coppola et al. (2012); (2015) took another step forward to allowed crack volume and/or hydrological  
93 properties to vary as a function of soil shrinkage. However, the relationship proposed in the model, a natural logarithm function  
94 involving the suction head and crack proportion, lacks physical consistency with the variation of porosity. This implies a  
95 disconnection between hydrological properties and porosity in the crack domain. Stewart et al. (2016b) deduced a shrinking-  
96 swelling model, with relatively clear physical meaning and high consistency, and recently incorporated it into a Green-Ampt  
97 based DPM (Stewart, 2018). While an analytical solution was obtained, the intrinsic limitation of the Green-Ampt approach  
98 (i.e. hypothesis of the wetting front and request for a constant boundary condition) hindered the further application of this  
99 model in complicated scenarios.  
100 The objective of this research was to investigate the PF-DC from the experimental perspective in combination with an  
101 effective modelling approach. Hence, a soil column test was conducted to investigate the dynamic changes of desiccation  
102 cracks and hydrological response. The variation of crack geometry, including crack ratio, width and depth were measured.  
103 The soil moisture content, matrix suction and water drainage were also monitored. Meanwhile, we developed a dynamic dual-  
104 permeability preferential flow model by incorporating the shrinking-swelling model proposed by Stewart et al. (2016b). The  
105 performance of the model was evaluated by comparing the simulated results with measured data.

## 106 2. Experimental study

### 107 2.1 Testing apparatus

108 To investigate the effects of dynamic changes of desiccation cracks on preferential flow, a soil column infiltration test was  
109 conducted under wetting-drying cycles (abbreviated as WD cycles hereafter). The testing apparatus consisted of a rainfall-  
110 evaporation system, environment monitoring device, a plexiglass column, HD camera, hydrological sensors and drainage  
111 measurement device (Fig. 1).

112 The rainfall-evaporation system included a rainfall simulator and two warm lamps as well as a small fan. The rainfall simulator  
113 was 0.5 m above the soil surface, which can produce rainfall with the intensity of 24-120 mm/h. The warm lamps and a small  
114 fan were put near the soil surface to accelerate water evaporation. The environment monitoring device consisted of a thermo-  
115 hygrometer that connected a probe above the soil surface to detect the environmental temperature and humidity, and a water  
116 container to measure the potential evaporation.

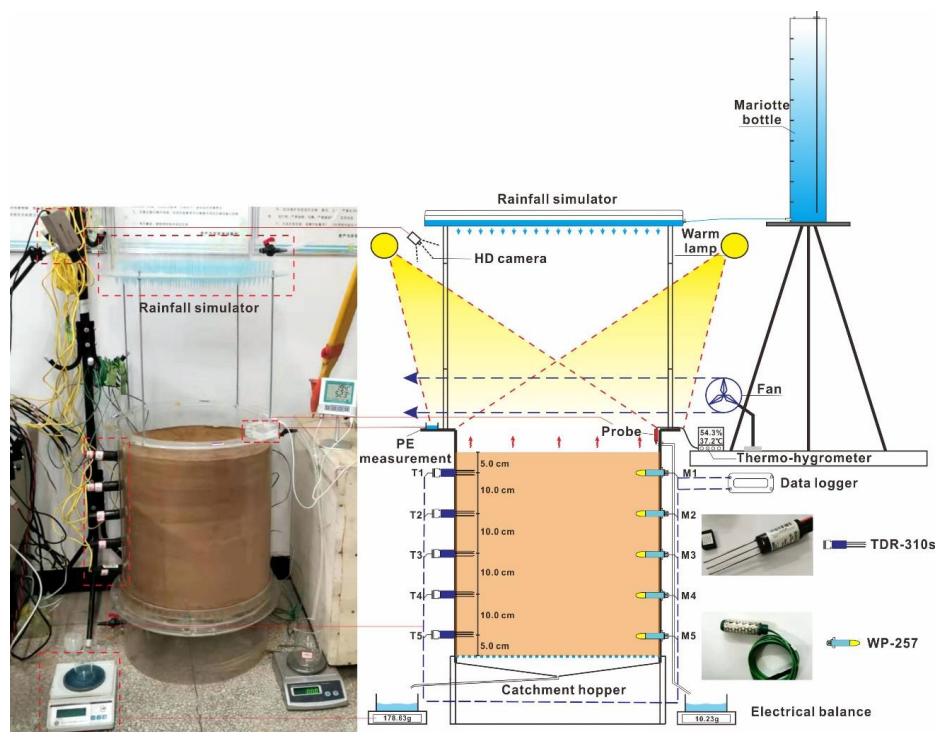
117 The plexiglass column was composed of a column (with a height of 60 cm and a diameter of 50 cm) placed on a catchment  
118 hopper which was used to collect and drain out water from the soil column.

119 HD camera (TTQ-J2, constant focal length: 35 mm) was fixed on the slope above the soil surface to take photos at regular  
120 intervals during the drying periods.

121 Hydrological sensors, including 5 soil moisture content/temperature sensors (Acclima, TDR-310s, with a measurement



122 moisture content range of 0-100%, an accuracy of  $\pm 2\%$ ; temperature range of  $-40\text{ }^{\circ}\text{C}$  -  $+60\text{ }^{\circ}\text{C}$ , an accuracy of  $\pm 0.2\text{ }^{\circ}\text{C}$ ) and 5  
 123 water potential sensors (Campbell, WP-257, with a measurement range of  $-200\text{ kPa}$  -  $0\text{ kPa}$ , an accuracy of  $\pm 0.5\text{ kPa}$ ), were  
 124 used to monitor the hydrological response during WD cycles. Five TDR-310s and five WP-257s were inserted into the soil  
 125 column from the two opposite sides of the plexiglass column, respectively, with the same height spacing of 10 cm from top  
 126 to bottom.  
 127 Drainage measurement device, including two electronic balances, were used to record the cumulative water drainage from  
 128 the soil column.



129  
 130 **Fig. 1** Schematic design and photos of the soil column test

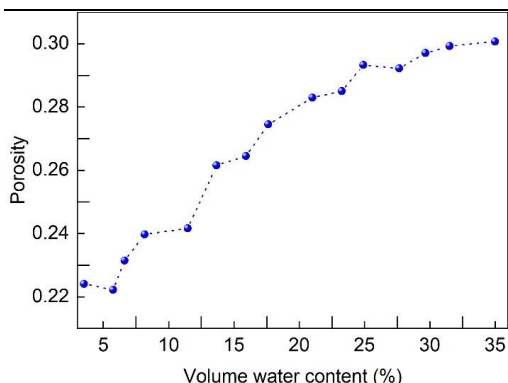
131 **2.2 Materials**

132 The soil used in the test was taken from Zongyang county Anhui, China. Table 1 shows the basic physical parameters and  
 133 main mineral composition of the soil samples. The soil found in this study is classified as weak expansive soil. The saturated  
 134 hydraulic conductivity was measured on reconstituted soil cores with a dry density of  $1.55\text{ g/cm}^3$  (the same as the soil column).  
 135 In addition, the shrinkage curve of the saturated soil core was also obtained using a similar method proposed in [Wen et al.](#)  
 136 [\(2021\)](#). The difference is that we measured the vertical deformation in regular time intervals instead of continuous monitoring.  
 137 Fig. 2 shows the variation of soil porosity with the volumetric water content.

138 **Table 1** Basic physical parameters of the soil sample

Gs (-)	$\omega_{opt}$	$\rho_{d,max}$	$L_l$ (%)	$P_l$ (%)	$\delta_{ef}$ (%)	$C_{Illite}$	$C_{Kaolinite}$	$C_{Quartz}$	$C_{Albite}$	$K_s$
2.73	0.17	1.7	38.7	18.9	42.7	43-57	4-12	34-47	0-11	$8.3 \times 10^{-7} - 1.3 \times 10^{-6}$

Gs - specific gravity (-);  
 $\omega_{opt}$  - optimal moisture content (g/g);  $\rho_{d,max}$  - the maximum dry density ( $\text{g/cm}^3$ );  
 $L_l$  - liquid limit (%);  $P_l$  - Plastic limit (%);  
 $\delta_{ef}$  - Free swelling ratio (%);  
 $C_{Illite}$ ,  $C_{kaolinite}$ ,  $C_{Quartz}$  and  $C_{Albite}$  - content of illite, kaolinite, quartz and albite, respectively (%);  
 $K_s$  - Saturated hydraulic conductivity (m/s)



139

140 **Fig. 2** Shrinkage curve of the test soil

141 To ensure the homogeneity of the soil column, soil samples were compacted in 10 layers, and each layer was 5 cm thick. Prior  
142 to filling soil into the plexiglass column, the soil samples with the total weight required for each layer were prepared according  
143 to the designed density (dry density of 1.55g/cm<sup>3</sup>) and gravimetric water content (10%). Then, the soil samples were  
144 compacted in the plexiglass column using a rubber hammer. The soil column was constructed within one day. After that, the  
145 soil column was allowed to stand for 3 days to obtain stable records of the hydrological sensors.

146

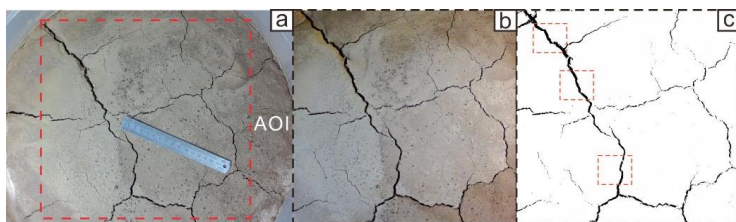
### 147 2.3 Data collection

148 In the soil column test, the following data was collected:

149 (1) Boundary conditions: rainfall intensity ( $r$ , mm/h), potential evaporation ( $PE$ , mm/h) at 1 h time interval, temperature ( $T$ , °C)  
150 and relative humidity ( $RH$ , %) at 5 min time interval.

151 (2) Hydrological data: volume water content ( $\theta_{exp}$ , %) and soil matrix suction ( $S_{exp}$ , kPa) in different depths at 5 min time  
152 interval, cumulative drainage from the top ( $D_{top}$ , g) and bottom ( $D_{bottom}$ , g) of the soil column.

153 (3) Crack geometric data: crack ratio ( $w_{c,exp}$ ), crack aperture ( $w_{j,exp}$ ), and the maximum crack depth ( $d_{max}$ , mm). The  $w_{c,exp}$   
154 and  $w_{j,exp}$  were obtained via processing the crack photos which were taken at 20 min intervals during drying periods. The  
155 image processing method mainly includes two steps as shown in Fig. 3. The  $d_{max}$  was measured by thin wire before each  
156 rainfall event.



157

158 Fig. 3 Process of crack image processing. (a) a photo obtained from the HD camera, 800 pixels × 1400 pixels; (b) crack  
159 image after cropping and pixel enhancement, 1044 pixels × 1005 pixels; (c) crack image after binarization and denoise, and  
160 the crack ratio was calculated as the crack area divided by the overall AOI area, the crack aperture was calculated as the  
161 average value of crack aperture from three different positions.

162

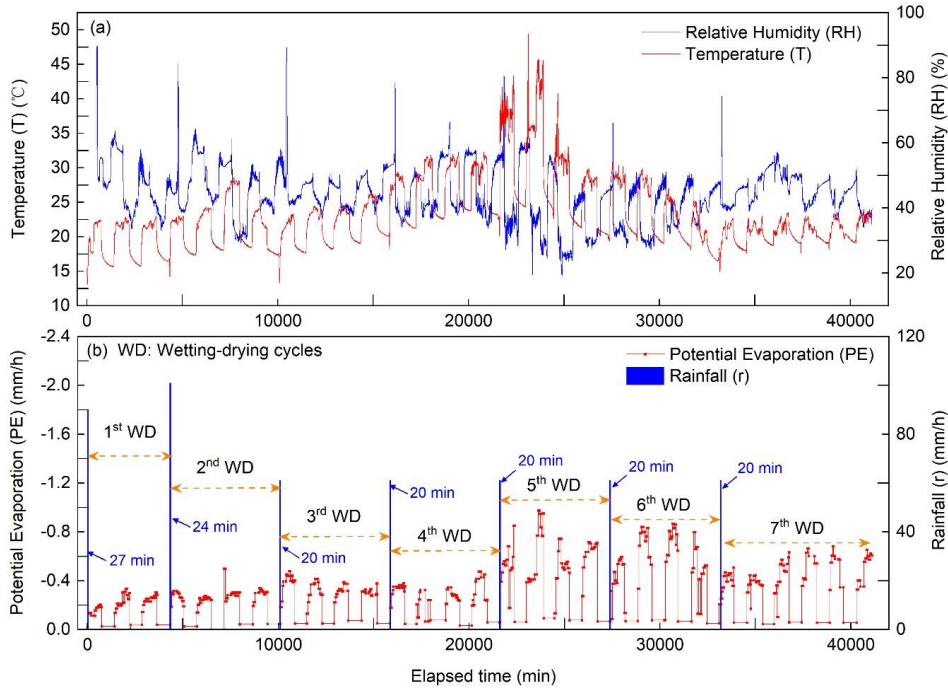
### 163 2.4 Test procedure

164 The overall experimental process included two stages of WD cycles. The purpose of the first stage was to generate a relatively  
165 stable surface pattern of the desiccation cracks. It started from 2022/01/05 15:00 to 2022/02/28 9:00, including thirteen WD  
166 cycles.





167 The second stage started from 2022/02/28 9:00 to 2022/03/28 22:30, including seven WD cycles. Fig. 4 presents the variation  
 168 of rainfall, evaporation, temperature and relative humidity in the entire experiment process. Because the two warm lamps and  
 169 fan were closed during the night, two kinds of evaporation intensity can be observed during the drying periods. In addition,  
 170 the average environment temperature in the 5<sup>th</sup> WD cycle was higher because we turned up the power of the two warm lamps.  
 171 In this current study, we mainly focus on the second stage of WD cycles.



172  
 173 **Fig. 4** Environmental conditions of the experiment. (a) time series of temperature and relative humidity; (b) rainfall intensity  
 174 and potential evaporation.  
 175

### 176 3. Model Description

#### 177 3.1 Dual-permeability model (DPM)

178 The DPM concept used in this study corresponds to the one developed by [Gerke and Van Genuchten \(1993a\)](#). The model  
 179 divides the flow domain into two overlapping and interacting continua according to the volumetric ratios of each domain,  
 180 where two coupled 2-D Richards' equations are used to describe the matrix flow and preferential flow as

$$181 \quad C_c(h) \frac{\partial h_c}{\partial t} = \nabla [K_c(h) \nabla (h_c + z)] - \frac{\Gamma_w}{w_c} \quad (1)$$

$$182 \quad C_m(h) \frac{\partial h_m}{\partial t} = \nabla [K_m(h) \nabla (h_m + z)] + \frac{\Gamma_w}{w_m} \quad (2)$$

$$183 \quad \Gamma_w = \alpha_w K_a (h_c - h_m) \quad (3)$$

$$184 \quad w_c + w_m = 1 \quad (4)$$

185 Where

186 subscript “c” and “m” indicate the crack and matrix domains, respectively;

187  $h$  (m) is the pressure head;

188  $C$  represents the specific water capacity,  $d\theta/dh$  (1/m);



189  $\theta$  (-) is the volumetric water content;  
190  $K$  (m/s) is the isotropic hydraulic conductivity;  
191  $z$  (m) is the elevation head;  
192  $w$  (-) is the volumetric ratio of the crack domain or matrix domain over the bulk soil volume;  
193  $\Gamma_w$  is the water exchange term (1/s) between the two domains;  
194  $\alpha_w$  (1/m<sup>2</sup>) is the effective water transfer coefficient;  
195  $K_a$  (m/s) is the interface hydraulic conductivity.  
196 The hydraulic properties of the two domains are parameterized based on the Mualem-van Genuchten soil-water retention  
197 curves (SWRC) (Mualem, 1976; Van Genuchten, 1980) as

$$198 \quad S_e(h) = \frac{\theta - \theta_r}{\theta_s - \theta_r} = [1 + (|\alpha h|)^n]^{-m} \quad (5)$$

$$199 \quad K(S_e) = K_s K_r(S_e) = K_s S_e^{0.5} [1 - (1 - S_e^{1/m})^m]^2 \quad (6)$$

200 where  $S_e$  (-) is the effective saturation;  $\theta_s$  (-) and  $\theta_r$  (-) are the saturated and residual volumetric water content, respectively;  
201  $\alpha$  (1/m),  $n$  (-) and  $m$  (-) are fitting parameters;  $K_s$  (m/s) is the saturated hydraulic conductivity;  $K_r$  (-) is the relative  
202 hydraulic conductivity.

203 According to Gerke and Van Genuchten (1993a), the total porosity  $\varepsilon$  (-), total volume water content  $\theta$  (-), total hydraulic  
204 conductivity  $K$  (m/s) and total volumetric flux (m/s) in terms of the volume ratio of each domain can be expressed as

$$205 \quad \varepsilon = w_c \varepsilon_c + w_m \varepsilon_m \quad (7)$$

$$206 \quad \theta = w_c \theta_c + w_m \theta_m \quad (8)$$

$$207 \quad K = w_c K_c + w_m K_m \quad (9)$$

208 Note that the total porosity  $\varepsilon$  is define as the total pore volume ( $V_p$ ) divided by total soil volume ( $V$ ), while  $\varepsilon_m$  (or  $\varepsilon_c$ ) is  
209 defined as the pore volume in matrix ( $V_{p,m}$ ) (or crack,  $V_{p,c}$ ) domain divided by the volume of that domain ( $V_m$  or  $V_c$ ). The total  
210 volume water content has the same definition.

211 In the case of a DPM model, specified flux  $i$  is divided between the matrix and crack domains as

$$212 \quad i = w_c i_c + w_m i_m \quad (10)$$

213 where  $i_c$  and  $i_m$  are the effective boundary fluxes into each domain (m/s).

214 Considering a rainfall condition, the effective boundary fluxes of the two domains are initially equal to rainfall intensity ( $r$ )  
215 due to the infiltration capacity of each domain is larger than  $r$  (Dusek et al., 2008), and therefore the boundary fluxes of each  
216 domain can be written as

$$217 \quad i_c = r \quad (11)$$

$$218 \quad i_m = r \quad (12)$$

219 As the soil keeps wetting, the decrease of the pressure head gradient may firstly lead to the infiltration capacity of matrix  
220 domain dropping to a value less than  $r$ . Then, ponding occurs on the surface of the soil matrix and the boundary condition  
221 changes to a specified pressure head boundary. This transformation can be achieved in COMSOL using a combined type of  
222 boundary (Dirichlet and Neumann) proposed by Chui and Freyberg (2009). Once ponding occurs on the matrix domain, the  
223 surplus water from that domain infiltrates into the crack domain and its effective flux increases to

$$224 \quad i_c = (r - w_m i_m) / w_c \quad (13)$$

225 when the retained water volume in the cracks exceeds its storage capacity, water will pond on the surface of the crack domain.  
226 Considering an evaporation condition, the Wilson-Fredlund-Barbour-Penman experimental function model (Wilson et al.,  
227 1997) was used to calculate the actual evaporation of each domain



$$228 \quad AE / PE = \exp\left(\frac{-Sg\omega_v}{\xi(1-h_a)\gamma_w R(T_s + 273.15)}\right) \quad (14)$$

229 Where

230 AE is the actual evaporation;

231 PE is the potential evaporation measured in the experiment;

232  $S$  (kPa) is total matric suction at the soil surface;

233  $g$  ( $\text{m/s}^2$ ) is the gravitational acceleration constant;

234  $\omega_v$  is molecular mass of water, 0.018kg/mol;

235  $\xi$  is a dimensional empirical parameter with a suggested value of 0.7;

236  $h_a$  is relative humidity of overlying air;

237  $\gamma_w$  is unit mass of water, 9.807 kN/m<sup>3</sup>;

238  $R$  is universal gas constant, 8.314J/(mol·K);

239  $T_s$  (°C) is the soil surface temperature.

240

241 3.2 Dynamic dual-permeability model (DPMDy)

242 3.2.1 Porosity description

243 In Stewart et al. (2016a); (2016b) and Stewart (2018), the total porosity ( $\phi_{\max}$ ) of a cracked soil was divided into three domains:  
 244 aggregates (or soil matrix), cracks (voids from horizontal deformation induced by desiccation cracks) and subsidence (voids  
 245 from vertical deformation induced by desiccation cracks). In Stewart et al. (2016a), the distributions of these domains change  
 246 as a function of a unified water content,  $U$

$$247 \quad \phi_{\max} = \phi_{\text{matrix}}(U) + \phi_{\text{crack}}(U) + \phi_{\text{sub}}(U) \quad (15)$$

248 where the subscripts matrix, crack and sub refer to the aforementioned three domains. In this study, we assume that the  
 249 horizontal deformation dominates the formation of desiccation cracks, thus  $\phi_{\text{sub}}(U)$  can be neglected.

250 Stewart et al. (2016a) then deduced the porosities of each domain as:

$$251 \quad \phi_{\text{matrix}}(U) = (\phi_{\max} - \phi_{\min}) \left( \frac{p+1}{p+U^{-q}} \right) + \phi_{\min} \quad (16)$$

$$252 \quad \phi_{\text{crack}}(U) = (\phi_{\max} - \phi_{\min}) \left( \frac{1-U^q}{1+pU^q} \right) \quad (17)$$

253 where  $p$  and  $q$  are functional shape parameters;  $\phi_{\max}$  is the maximum porosity of a soil core prior to shrinkage and thus also  
 254 represents the total porosity;  $\phi_{\min}$  is the minimum porosity of the matrix domain;  $U$  is a unified water content (defined as  
 255 water content  $u$  divided by its saturated value  $u_{\max}$ ), which can be approximately estimated to be the saturation degree ( $S_{e,m}$ )  
 256 in an SWRC function of the soil matrix (Stewart et al., 2016a). Indeed, Eq. (16) represents a shrinkage curve function in which  
 257 four parameters can be obtained through a shrinkage test.

258 Substituting  $S_{e,m}$  as  $U$  and incorporating Eq. (5) into Eq. (16) and Eq. (17), we can obtain the porosity of the two domains as  
 259 a function of pressure head  $h$

$$260 \quad \phi_{\text{matrix}}(h) = (\phi_{\max} - \phi_{\min}) \left( \frac{p+1}{p+S_{e,m}^{-q}} \right) + \phi_{\min} = (\phi_{\max} - \phi_{\min}) \left( \frac{p+1}{p + \left( [1 + (|\alpha_m h_m|)^{n_m}]^{-m_m} \right)^{-q}} \right) + \phi_{\min} \quad (18)$$

$$261 \quad \phi_{\text{crack}}(h) = (\phi_{\max} - \phi_{\min}) \left( \frac{1-S_{e,m}^q}{1+pS_{e,m}^q} \right) = (\phi_{\max} - \phi_{\min}) \left( \frac{1 - \left( [1 + (|\alpha_m h_m|)^{n_m}]^{-m_m} \right)^q}{1 + p \left( [1 + (|\alpha_m h_m|)^{n_m}]^{-m_m} \right)^q} \right) \quad (19)$$





262 With these porosity equations in mind, we can rewrite Eq. (4) and Eq. (7) as:

263 
$$\phi_{\max} = w_c \varepsilon_c + (1 - w_c) \varepsilon_m \quad (20)$$

264 Because the crack domain is mainly composed of voids, we here assume that  $V_{p,c}$  equals to  $V_c$ , and thus  $\varepsilon_c = 1$ . Through this  
 265 assumption, we obtained a physically-consistent definition of how the porosity and crack volume vary as functions of  
 266 saturation degree as follow

267 
$$w_c \varepsilon_c = w_c = \phi_{crack}(S_{e,m}) = (\phi_{\max} - \phi_{\min}) \left( \frac{1 - S_{e,m}^q}{1 + p S_{e,m}^q} \right) \quad (21)$$

268 
$$\varepsilon_m = \frac{\phi_{matrix}(S_{e,m})}{1 - w_c} = \left[ (\phi_{\max} - \phi_{\min}) \left( \frac{p+1}{p + S_{e,m}^{-q}} \right) + \phi_{\min} \right] / \left[ 1 - (\phi_{\max} - \phi_{\min}) \left( \frac{1 - S_{e,m}^q}{1 + p S_{e,m}^q} \right) \right] \quad (22)$$

269

### 270 3.2.2 Water content and hydraulic conductivity

271 In terms of Eq. (8), the total water content of the soil volume can be expressed as:

272 
$$\theta = \phi_{crack}(h) \theta_c + (1 - \phi_{crack}(h)) \theta_m \quad (23)$$

273 Regarding the hydraulic conductivity of each domain, the classical DPM often assumed it equals to the product of a fixed  $K_s$   
 274 and the relative hydraulic conductivity of the corresponding domain. The following equations are obtained according to Eq.  
 275 (6).

276 
$$K_m = K_{m,s} K_r(S_{e,m}) = K_{m,s} S_{e,m}^{0.5} [1 - (1 - S_{e,m}^{1/m_m})^{m_m}]^2 \quad (24)$$

277 
$$K_c = K_{c,s} K_r(S_{e,c}) = K_{c,s} S_{e,c}^{0.5} [1 - (1 - S_{e,c}^{1/m_c})^{m_c}]^2 \quad (25)$$

278 where  $K_{c,s}$  and  $K_{m,s}$  refer to the saturated hydraulic conductivity in crack and matrix domains, respectively.

279 However, the  $K_{c,s}$  and  $K_{m,s}$  are transient variables that changes with the crack geometries in crack domain and porosity in  
 280 matrix domain, which should be taken into consideration in a shrinking-swelling soil. To solve this issue, [Stewart et al. \(2016b\)](#)  
 281 further deduced models that describe the relationships between  $K_{m,s}$ ,  $K_{c,s}$  and  $S_{e,m}$ .

282 
$$K_{m,s}(S_{e,m}) = K_{m,\max} \left( \frac{p+1}{p + S_{e,m}^{-q}} \right) \quad (26)$$

283 
$$K_{c,s}(S_{e,m}) = K_{c,\max} \left( \frac{1 - U^q}{1 + p S_{e,m}^q} \right)^2 \quad (27)$$

284 where  $K_{c,\max}$  is the maximum saturated hydraulic conductivity of the crack domain (at  $S_{e,m} = 0$ ) when the crack aperture  
 285 achieves the maximum value;  $K_{m,\max}$  is the maximum saturated hydraulic conductivity of the matrix domain (at  $S_{e,m} = 1$ )  
 286 when the radius of cylindrical pores in that domain achieves the maximum value (See Eq. (25) and Eq. (27) in [Stewart et al.](#)  
 287 [\(2016b\)](#)). In the DPMDy model, we here set  $K_r(S_{e,c})$  to 1 in Eq. (25). This modification means that the magnitude of  $K_c$   
 288 only depends on the crack area or the saturated degree of the soil matrix domain.

289 
$$K_c = K_{c,s} = K_{c,s}(S_{e,m}) = K_{c,\max} \left( \frac{1 - U^q}{1 + p S_{e,m}^q} \right)^2 \quad (28)$$

290 Incorporating Eq. (26) and Eq. (27) into Eq. (9) obtains:



$$K_s = \phi_{crack}(h) K_{c,max} \left( \frac{1 - S_{e,m}^{-q}}{1 + p S_{e,m}^{-q}} \right)^2 + (1 - \phi_{crack}(h)) K_{m,max} \left( \frac{p+1}{p + S_{e,m}^{-q}} \right) \quad (29)$$

Note that  $K_{m,max}$  can be obtained by laboratory-based infiltration test through a saturated soil core prior to shrinkage. Then, Eq. (29) can be used to fit the  $K_{c,max}$  through the overall saturated hydraulic conductivity (measured  $K_s$ ) under different crack volume or ratio. Alternatively,  $K_{c,max}$  can also be approximately calculated as

$$K_{c,max} = \frac{w_{j,max}^2 g}{12\nu} \quad (30)$$

where  $w_{j,max}$  stands for the maximum crack aperture measured in experiment (m),  $g$  is the gravity acceleration constant ( $m/s^2$ ), and  $\nu$  is the water kinematic viscosity ( $m^2/s$ ). This equation is a relation to the cubes of the aperture of a crack with respect to the crack inner flux, which is based on the derivation of laminar flow between parallel plates for Hagen-Poiseuille type of flow (Snow, 1965).

Eventually, we can simulate the hydrological process with considering the dynamic changes of desiccation cracks by incorporating Eq. (19), Eq. (21), Eq. (26), Eq. (27) and Eq. (28) into the DPM.

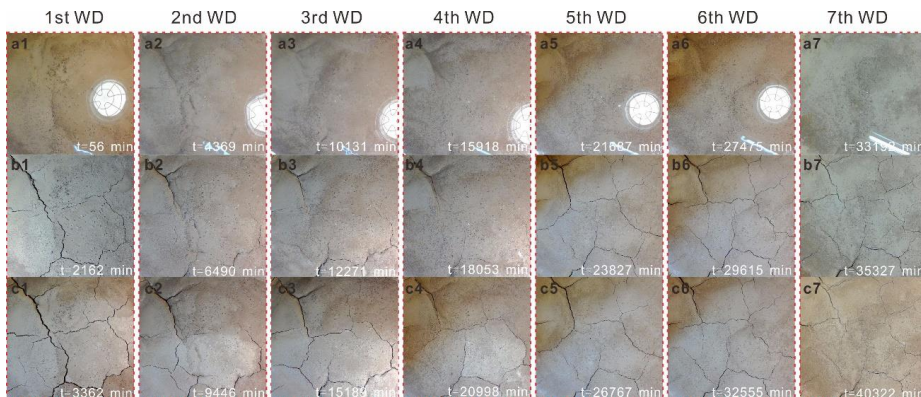
302

#### 303 4. Experimental results

##### 304 4.1 Crack dynamic changes

Fig 5 presents typical images of crack evolution during each WD cycle. Intuitively, it seems that the crack area and width did not show an obvious increasing trend with the WD cycles as expected. Conversely, during the 1<sup>st</sup> to 4<sup>th</sup> WD cycles, the cracks at the same moment after rainfall (Fig 5b2-4) and the final state (Fig 5c2-4) decreased significantly even though the environmental temperature ( $T$ ) and the potential evaporation ( $PE$ ) increased in these periods. The cracks increased significantly since the 5<sup>th</sup> WD cycle, but most of them were finer than before. Overall, cracks in the 1<sup>st</sup> WD cycle are wider than those formed in other cycles.

310



311

**Fig. 5** Typical images of crack evolution in seven wetting-drying cycles. (a1-7) water ponds on the soil surface after rainfall; (b1-7) crack images at the 2135<sup>th</sup> min after each rainfall; (c1-7) crack images at the end of the final high evaporation period during each wetting-drying cycle

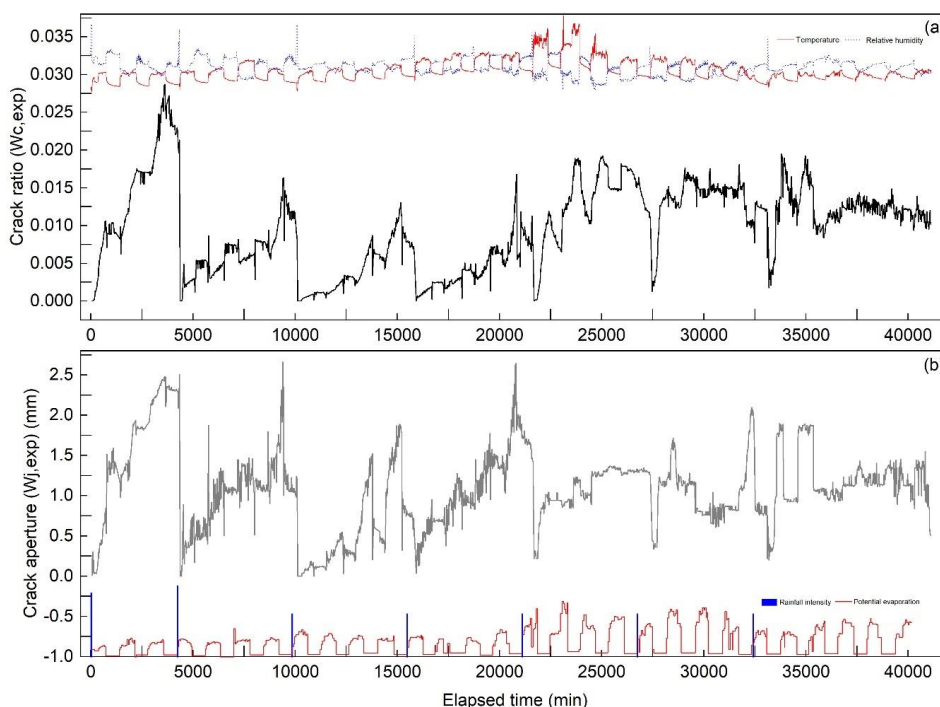
315

Fig 6 quantitatively shows the variation of crack ratio ( $w_{c,exp}$ ) and crack aperture ( $w_{j,exp}$ ) in the experiment. Overall, the variation curves corresponded to the intuitive descriptions mentioned above. Especially, an unexpected result was that the  $T$

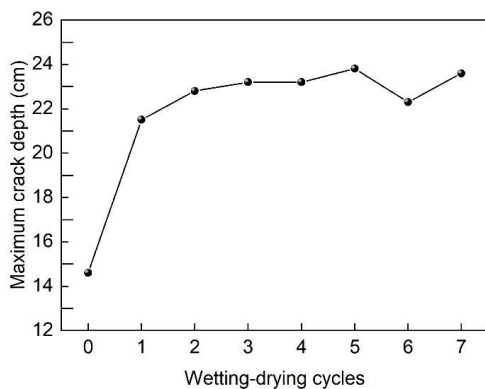
317



318 and  $PE$  in the 5<sup>th</sup> and 6<sup>th</sup> WD cycles were higher than in previous cycles, but their maximum  $w_{c,exp}$  and  $w_{j,exp}$  became  
 319 smaller. During a single WD cycle, the  $w_{c,exp}$  and  $w_{j,exp}$  have a similar trend, which shows a dramatic decrease during  
 320 rainfall, rapid increase in high evaporation periods and slow increase or even decrease in low evaporation periods. More  
 321 specifically, during the rainfall periods, the crack closure process was not significant until the water ponded on the soil matrix,  
 322 then ponded water flowed into the cracks, leading to acceleration of the crack closure. Note that cracks were not completely  
 323 closed even when they were full of water (Fig 5a1-7). The minimum crack ratio under such conditions is approximately 0.1%.  
 324 In the evaporation periods, the maximum crack ratio reaches 2.87% and the maximum crack aperture reaches 2.6 mm. In  
 325 addition, Fig 7 shows the maximum crack depth ( $d_{max}$ ) measured after each cycle. It can be seen that  $d_{max}$  increased  
 326 substantially after the 1<sup>st</sup> WD cycle and then slightly increased in the last six cycles, with a maximum value of 23.8 cm.



327  
 328 **Fig. 6** Time series of crack geometries. (a) crack ratio; (b) crack aperture



329  
 330 **Fig. 7** The maximum crack depth measured after each wetting-drying cycle

331  
 332 4.2 Hydrological response

333 Table 2 presents the manually recorded results of external hydrological responses involving ponding and drainage during each

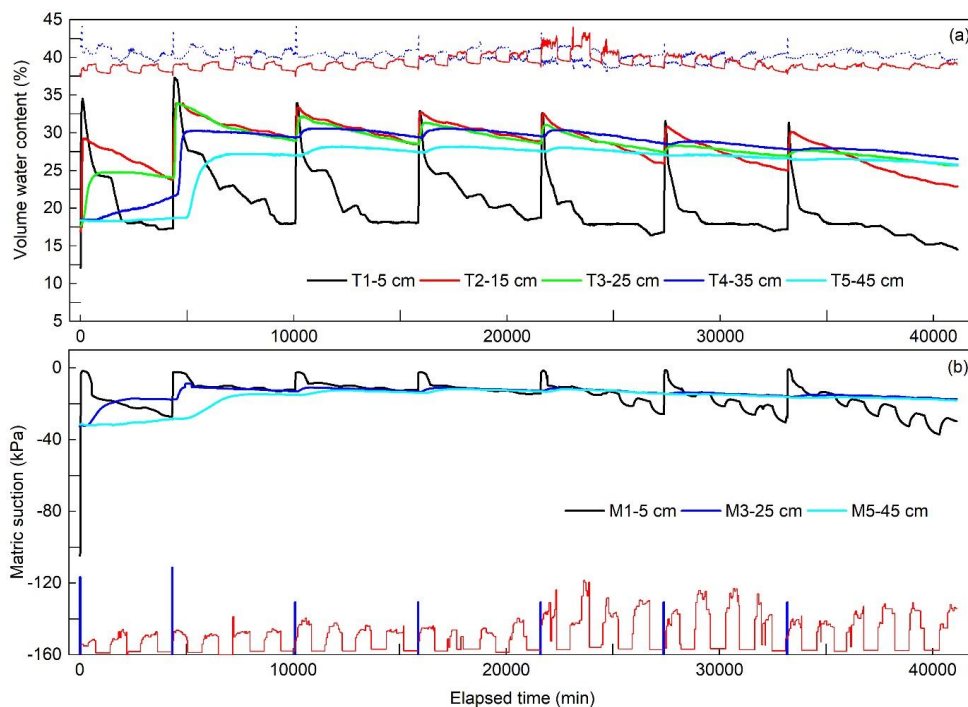


334 WD cycle. It can be seen that the ponding occurred on the soil surface within 5 min after each rainfall. The ponding duration  
 335 in each rainfall mainly decreased with WD cycles. Note that the ponding depth in each rainfall was below the upper drainage  
 336 outlet. Regarding the water drainage, approximately 1.4 kg of water (the total water mass was 8 kg) was leaked during the 1<sup>st</sup>  
 337 rainfall due to the interspace between the soil and the plexiglass column and the hydrological sensors. Then, we sealed the  
 338 interspace using clay powder and polyurethane cement (soft materials without constrain effects on the soil swelling) after  
 339 each drying process, and subsequently, no water drainage was observed at the bottom outlet.

340 **Table 2** Statistical results of external hydrological responses

Wetting-drying cycles	1 <sup>st</sup>	2 <sup>nd</sup>	3 <sup>rd</sup>	4 <sup>th</sup>	5 <sup>th</sup>	6 <sup>th</sup>	7 <sup>th</sup>
$t_p$ (min)	4.1	1.8	1.2	1.2	1.2	2.2	2.8
Ponding duration (min)	70	160	68	47	34	25	23
Drainage (g)	1412	-	-	-	-	-	-
* $t_p$ (min) – beginning of ponding after each rainfall							

341 Fig 8 shows the internal hydrological responses recorded by the soil moisture and water potential sensors. Because the M2  
 342 and M4 were damaged during soil compaction, no matric suction data was obtained at their depths. Overall, water content at  
 343 all depths increased during rainfall and decreased during evaporation, where T1 showed the most sensitive responses to the  
 344 WD cycles. During rainfall, the time for water content to respond to each rainfall increased with depths, but the time difference  
 345 among all depths decreased significantly since the 2<sup>nd</sup> WD cycle. During the drying periods, an interesting phenomenon was  
 346 that the water content at 5 cm depth showed an overall decline trend, but transient increases of water content frequently  
 347 appeared during low evaporation periods. Such transient increases seem to be related to the slow decrease of crack ratio as  
 348 mentioned in section 4.1. Regarding the matric suction, its variation trend was similar to the water content but showed more  
 349 delayed responses to the environmental conditions, especially in the last three WD cycles. Additionally, Fig 8b also implies  
 350 that soil at 5 cm depth reached saturation during each rainfall, while soil below the 25 cm depth was in the unsaturated state  
 351 in the whole experiment process.



352  
 353 **Fig.8** Time series of volume water content (a) and matric suction (b) at different depths.  
 354



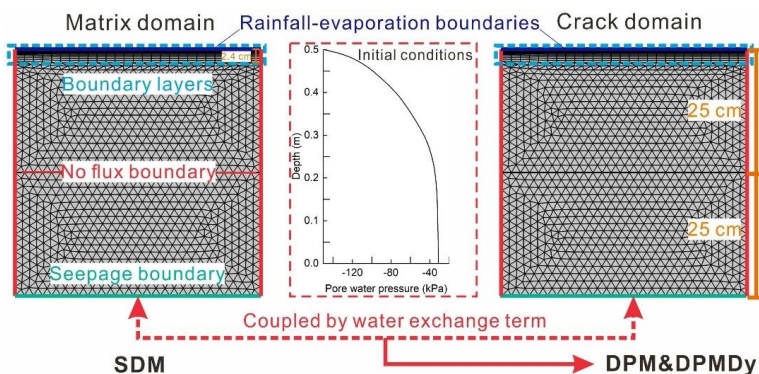
355 **5. Numerical simulation**

356 5.1 Set-up of numerical model

357 The single-domain model (SDM), dual-permeability model (DPM) and dynamic DPM (DPMDy) were implemented in a finite  
 358 element solver for Richards' equation as part of the COMSOL Multiphysics software (Comsol 5.6). As shown in Fig 9, they  
 359 have the same 2-D size, boundary conditions, mesh structure and initial condition. The model domain is 0.5 m by 0.5 m, same  
 360 as the soil column. Because the measured maximum crack depth was 23.8 cm, we specified the crack domain existing within  
 361 the upper 25 cm depth of the soil column.

362 The boundary conditions at the top were set as combined type of boundary conditions (as mentioned in section 3.1) for  
 363 representing the rainfall, ponding and evaporation process recorded in the experiment; the bottom side is a seepage boundary  
 364 condition; the left and right sides of the model are no-flux boundaries.

365 Because the pressure head in the surface area may change frequently and drastically during WD cycles, a refined mesh  
 366 structure with dense boundary layers was used to capture the transient hydrological conditions. The boundary layers included  
 367 15 layers of rectangular grid, with the minimum and maximum thick of approximately 0.04 cm and 0.3 cm, respectively. A  
 368 coarser free-triangle mesh (average length of 1.8 cm) was defined below the boundary layers. The initial condition both in  
 369 matrix and crack domains was set as the distribution of pore water pressure measured from the experiment prior to the 1<sup>st</sup> WD  
 370 cycle.



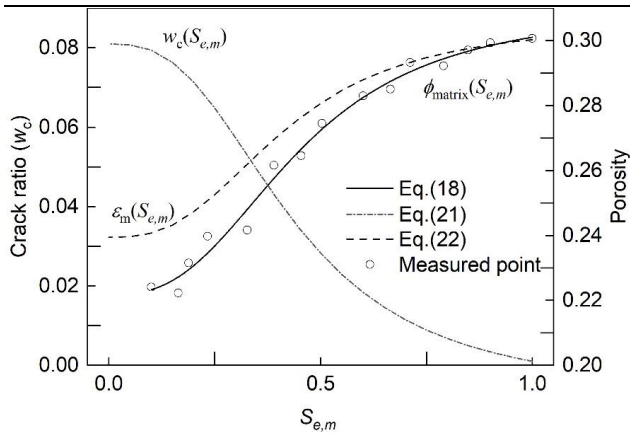
371 **SDM** **DPM&DPMDy**  
 372 **Fig. 9** Set-up of the 2-D numerical model for the SDM, DPM and DPMDy

374 5.2 Parameters

375 5.2.1 Shrinkage parameters

376 As shown in Fig 10, using Eq. (18) to fit the measured shrinkage curve in Fig. 2, we obtained the four shrinkage parameters  
 377 as  $\phi_{\min}=0.22$ ,  $\phi_{\max}=0.30$ ,  $p=8.8 \pm 4.84$ ,  $q=2.71 \pm 0.85$ . Then, the variation of porosity in crack domain (or crack ratio  
 378  $w_c$ ) and matrix domain ( $\varepsilon_m$ ) could be obtained using Eq. (21) and Eq. (22), respectively. Note that the minimum  $w_c$  calculated  
 379 by Eq. (21) was set as 0.001 considering the incomplete closure of cracks during rainfall.





380  
 381 **Fig. 10** Fitted shrinkage curve (solid line) and modeled porosity variation of matrix (dash line) and crack domains (dash-dot  
 382 line)  
 383

#### 384 5.2.2 Soil water retention parameters

385 **Fig 11** shows the measured matric suction versus volume water content (or measured SWRC) at different depths. It can be  
 386 seen that the WD cycles lead to hysteretic curves in the SWRC at 5 cm and 25 cm depths, while that at the 45 cm depth rarely  
 387 show hysteretic curves. This result may also indicate that most of the cracks exist within the upper 25 cm depth of the soil  
 388 column. In this study, we simply estimated an approximate single SWRC of the soil matrix through experiment data instead  
 389 of incorporating the hysteretic curves into the model. For instance, the estimated SWRC curve in **Fig 11a** lies between the  
 390 wetting SWRC and drying SWRC to capture the overall characteristics of wetting-drying SWRC as far as possible. Note that  
 391 the shape parameter  $n$  in the upper matrix domain is slightly smaller than the lower one considering the upper soil matrix may  
 392 become denser after long-time WD cycles (13 times, 54 days). Regarding the SWRC of the crack domain with macropore-  
 393 dominated space, the SWRC parameters of that domain were set with a greater saturated water content ( $\theta_{c,s} = 0.99$ ), a lower  
 394 value of air entry pressure ( $\alpha = 1.5$ ) and a steeper slope ( $n_c = 2$ ) than that of the matrix domain.

395

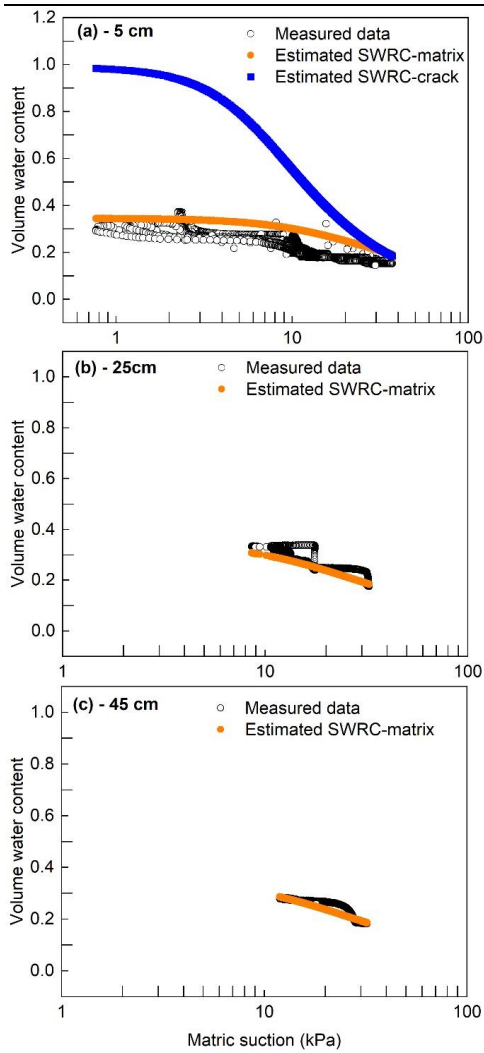
#### 396 5.2.3 Hydraulic conductivity

397 As mentioned in Eq. (29), the maximum saturated hydraulic conductivity of matrix domain ( $K_{m,max}$ ) equals the saturated  
 398 hydraulic conductivity ( $K_s$ ) measured in laboratory. Here, we set  $K_{m,max} = 1.16 \times 10^{-6}$  m/s. Regarding the  $K_{c,max}$ , it was  
 399 calculated using Eq. (30), where the  $w_{j,max}$  was set to 2.6 mm obtained from Fig 6b. Then, the variation curve of transient  
 400 saturated hydraulic conductivity of the matrix domain ( $K_{m,s}$ ) and the crack domain ( $K_{c,s}$ ) could be obtained using Eq. (27)  
 401 and Eq. (28), respectively. Note that here we slightly modified Eq. (28) as follow.

$$402 \quad K_{c,s}(S_{e,m}) = K_{c,max} \left( \frac{1 - S_{e,m}^q}{1 + p S_{e,m}^q} \right)^2 + K_{c,min} \quad (28-b)$$

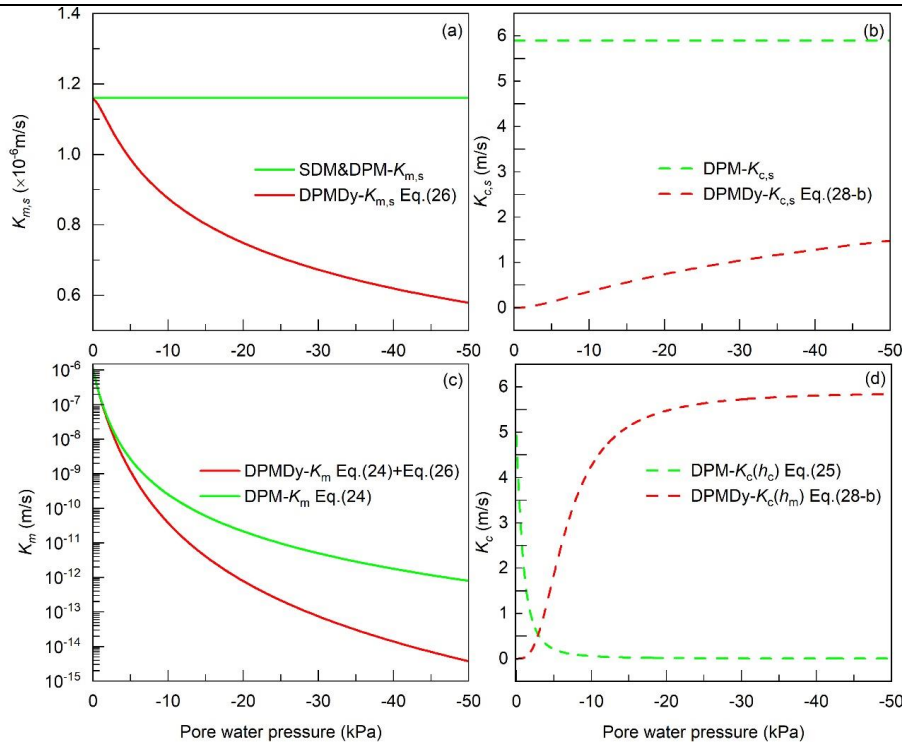
403 This modification not only avoided the  $K_{c,s}$  dropping to zero thus benefits the numerical convergence, but also was  
 404 reasonable when considering the incomplete closure of cracks during rainfall. The  $K_{c,min}$  was also estimated using Eq. (30)  
 405 with a suggested  $w_{j,max} = 0.01$  mm. Further, the variation of  $K_m$  and  $K_c$  with the pressure head ( $h$ ) in the DPMDy could  
 406 be calculated by combining Eq. (24), Eq. (26) and Eq. (28). **Fig 12** presents  $K_m$  and  $K_c$  in the three models. Note that the  
 407 pressure head in  $K_c(h_m)$  of the DPMDy refers to that of the matrix domain ( $h_m$ ), while  $h$  in  $K_c(h_c)$  of the DPM refers to  
 408 that of the crack domain ( $h_c$ ).





409

410 **Fig. 11** Measured and estimated SWRC at different depths. (a) 5 cm; (b) 25 cm; (c) 45 cm



411  
 412 **Fig. 12** Modeled hydraulic conductivity of each domain in the three models. (a) Saturated hydraulic conductivity of the matrix  
 413 domain; (b) saturated hydraulic conductivity of the crack domain; (c) transient hydraulic conductivity of the matrix domain;  
 414 (d) transient hydraulic conductivity of the crack domain  
 415

416 In the dual-permeability concept, another important parameter is the hydraulic conductivity of the interface between matrix  
 417 and crack domains ( $K_a$ ). Generally,  $K_a$  was often estimated as the arithmetic mean of hydraulic conductivity of the two domains  
 418 (Arora et al., 2011; Coppola et al., 2012; 2015; Gerke and Van Genuchten, 1993b; Laine-Kaulio et al., 2014; Shao et al., 2015).  
 419 However, this approximation may overestimate the  $K_a$  when the hydraulic conductivity of the crack domain is much higher  
 420 than that of the matrix domain, especially in cracked clays. In our current study, a  $K_a$  function reformulated by (Gerke et al.,  
 421 2013) was adopted.

$$422 \quad K_{a_{\min}} = \begin{cases} \min\{K_m(h_c), K_c(h_c)\} & h_c \geq h_m \\ \min\{K_m(h_m), K_c(h_m)\} & h_c < h_m \end{cases} \quad (31)$$

423 This formulation represents that the flow occurs from the highest head toward the lowest head but regulated by the less  
 424 permeable of the two subsystems in that instant of time (Aguilar - López et al., 2020).

425 Regarding the  $\alpha_w$ , experimental results presented by Song et al. (2018) showed that the saturated  $K_a$  may be 1 order of  
 426 magnitude larger than the  $K_{m,s}$  which will represent an enlarging coefficient ranging from 10 to 18. Hence, the  $\alpha_w$  was set  
 427 as  $10 \text{ m}^{-2}$  considering the saturated  $K_{a_{\min}}$  determined by Eq. (31) equals to the  $K_{m,s}$ .

428 All parameters for the SDM, DPM and DPMDy are listed in **Table 3**.

429 **Table 3** Summary of parameters for the SDM, DPM and DPMDy

Model	Symbol	Parameter name	Units	Upper layer	Lower layer
SDM	$\theta_{m,s}$	Saturated water content of matrix domain	(-)	0.345	0.345
DPM	$\theta_{m,r}$	Residual water content of matrix domain	(-)	0.01	0.01



DPMDy	$\alpha_m$	Mualem-van Genuchten fitting parameter of matrix domain	(1/m)	0.6	0.6
	$n_m$	Mualem-van Genuchten fitting parameter of matrix domain	(-)	1.65	1.8
	$K_{m,max}$	The maximum $K_s$ of matrix domain before shrinkage	(m/s)	$1.16 \times 10^{-6}$	$1.16 \times 10^{-6}$
DPM DPMDy	$\theta_{c,s}$	Saturated water content of crack domain	(-)	0.99	-
	$\theta_{c,r}$	Residual water content of crack domain	(-)	0.01	-
	$\alpha_c$	Mualem-van Genuchten fitting parameter of crack domain	(1/m)	1.5	-
	$n_c$	Mualem-van Genuchten fitting parameter of crack domain	(-)	2	-
	$K_{c,max}$	The maximum $K_s$ of crack domain	(m/s)	5.9	-
	$K_a$	Hydraulic conductivity of the interface	(m/s)	$K_{amin}$	-
	$a_w$	Mass transfer coefficient	(1/m <sup>2</sup> )	10	-
DPMDy	$\phi_{max}$	The maximum porosity of a soil core before shrinkage	(-)	0.3	-
	$\phi_{min}$	The minimum porosity of a soil core after shrinkage	(-)	0.22	-
	p	Shape parameter of soil shrinkage curve in Eq. (18)	(-)	10	-
	q	Shape parameter of soil shrinkage curve in Eq. (18)	(-)	3.5	-
DPM	$w_c$	Constant crack ratio using in DPM	(-)	0.01; 0.03	-

\* SDM: single-domain model; DPM: dual-permeability model neglecting crack dynamic changes; DPMDy: Dynamic DPM;  $w_c = 0.01$  and  $0.03$  refers to the average and the maximum value of the measured crack ratio, respectively.

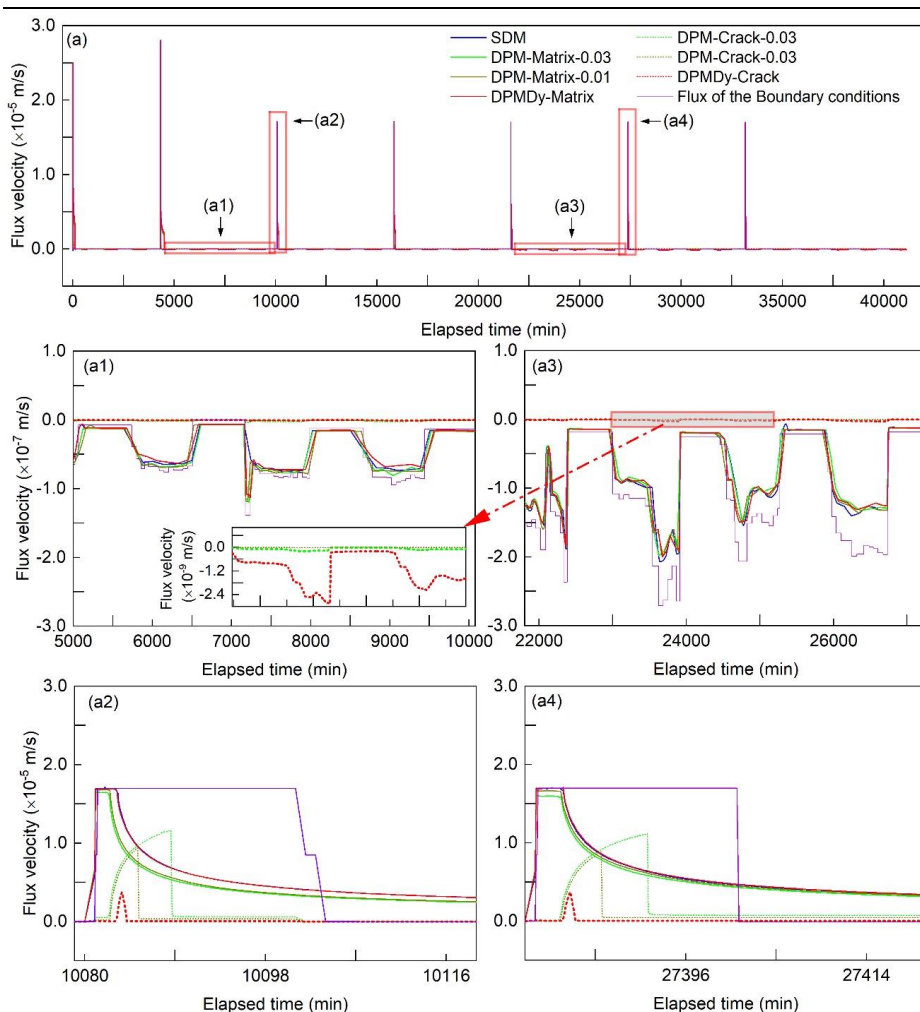
430

### 431 5.3 Simulation results

#### 432 5.3.1 Boundary flow

433 **Fig. 13** shows the temporal evolution of the boundary flow velocity simulated by the SDM, DPM and DPMDy. As shown in  
 434 **Fig. 13a1 and a3**, during drying periods, the matrix domain dominates the soil evaporation process and was responsible for  
 435 97%-99% of the total evaporation in all the dual-permeability models. The matrix evaporation rate ( $\epsilon_m$ ) simulated by the  
 436 DPMDy was overall lower than that of the SDM and DPM during high-intensity evaporation periods, but the crack  
 437 evaporation rate ( $\epsilon_c$ ) simulated by the DPMDy, especially during the last three drying periods, was approximately one to two  
 438 orders of magnitude larger than that of the DPM (see the enlarged image in Fig. a1).

439 With regard to the wetting process, **Fig. 13a2 and a4** represent two typical infiltration patterns before and after the 5<sup>th</sup> drying  
 440 period (with significantly increased evaporation intensity). Overall, matrix flow still dominated the infiltration process in all  
 441 the dual-permeability models due to the relatively small crack ratio and depth. For the SDM, all the rainfall infiltrates into the  
 442 soil during the beginning of rainfall events. When the soil surface gets saturated, water ponding occurred and the soil infiltration  
 443 rate gradually decreased. In the DPM and DPMDy, the surplus water after matrix ponding infiltrates into the crack domain as  
 444 preferential flow, and water will pond on the overall soil surface when the crack domain reached its storage capacity. Recall  
 445 that the crack volume in the DPMDy decreases with the matrix getting moist, while that in the DPM keeps constant.  
 446 Consequently, the ponding time of the crack domain simulated by the DPMDy in the 3<sup>rd</sup> rainfall event (inflection point of the  
 447 red dash line in Fig. 13a2) was 1.6 and 4.8 min earlier than that of the DPM-0.01 and DPM-0.03, respectively. The cumulative  
 448 preferential flow simulated by the DPMDy was 87.4% and 95.2 % less than that of the DPM-0.01 and DPM-0.03, respectively.  
 449 Similar rainfall pattern was obtained during the 6<sup>th</sup> rainfall event.



450  
 451 **Fig. 13** Boundary flow simulated by the SDM, DPM and DPMDy. (a) Flow velocity of the boundary conditions and simulated  
 452 results; (a1) and (a2) are the enlarged images of the flow velocity during the 2<sup>st</sup> drying and 3<sup>rd</sup> wetting process, respectively;  
 453 (a3) and (a4) are the enlarged images of the flow velocity during the 5<sup>th</sup> drying and 6<sup>th</sup> wetting process, respectively. The  
 454 positive value is for infiltration and negative for evaporation.

455

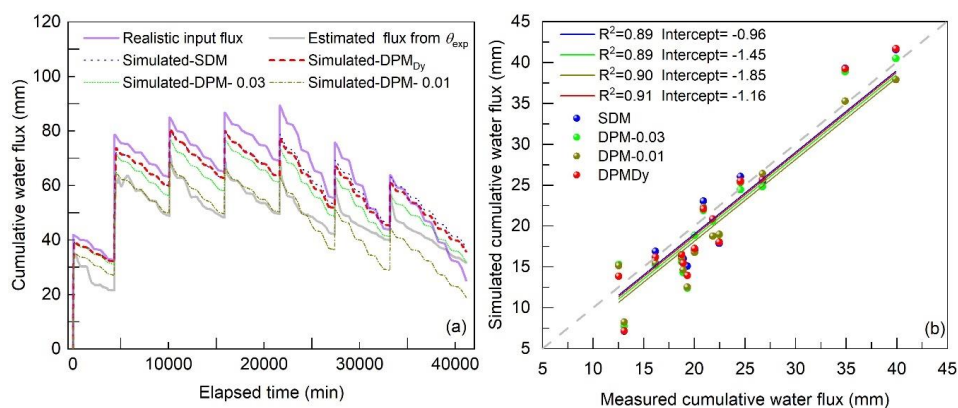
### 456 5.3.2 Water balance

457 By integrating the boundary flow velocity in Fig. 13a, the total cumulative flux for the experiment and the three models were  
 458 obtained (**Fig 14a**). In the experiment, the variation of water flux was estimated by calculating the sum of the difference  
 459 between  $\theta_{ini}$  (initial volume water content) and  $\theta_{t=i}$  (volume water content at any time) in the five monitoring depths.  
 460 Meanwhile, the water evaporation during water ponding was also estimated and added to the total flux volume. Regarding  
 461 the numerical model, the water balance was obtained by integrating all flow components along the upper and lower boundaries.  
 462 The steep increase stage of each curve represents cumulative input water flux during wetting periods and the gradual decrease  
 463 stage represents cumulative output water flux during drying periods. To evaluate the performance of each model on the water  
 464 balance, the measured cumulative input and output water fluxes in each wetting and drying stage were compared to the  
 465 simulated ones (Fig. 14b).

466 In Fig. 14a, the results show that the total infiltration ( $I_{t,inf}$ ) and evaporation flux ( $E_{t,eva}$ ) estimated from measured  $\theta_{exp}$  were



467 171 mm and 138.95 mm, respectively. The  $I_{t,inf}$  was 5.86 % less than the supplied water (183.44 mm) due to the water leakage.  
 468 The  $E_{t,eva}$  was 16.48 % less than the cumulative  $PE$  (166.36 mm) because of the limit of the soil actual evaporation. Regarding  
 469 the simulation results, the coefficient of determination ( $R^2$ ) and intercept were used to evaluate the errors made by the three  
 470 models. As shown in Fig. 14b, the slope of each fitting curve was fixed as 1. The SDM and DPMDy have relatively smaller  
 471 intercepts and slightly higher  $R^2$  than that of the DPM-0.01 and DPM-0.03, indicative of a better coincidence to the measured  
 472 data. Overall, the errors in water balance caused by the three models were acceptable in this study.



473  
 474 **Fig. 14.** Water balance for the measured and simulated results (a) Temporal evolution of total water flux calculated from the  
 475 measured water content, SDM, DPM and DPMDy; (b) measured versus modeled cumulative flux during each drying and  
 476 wetting stage  
 477

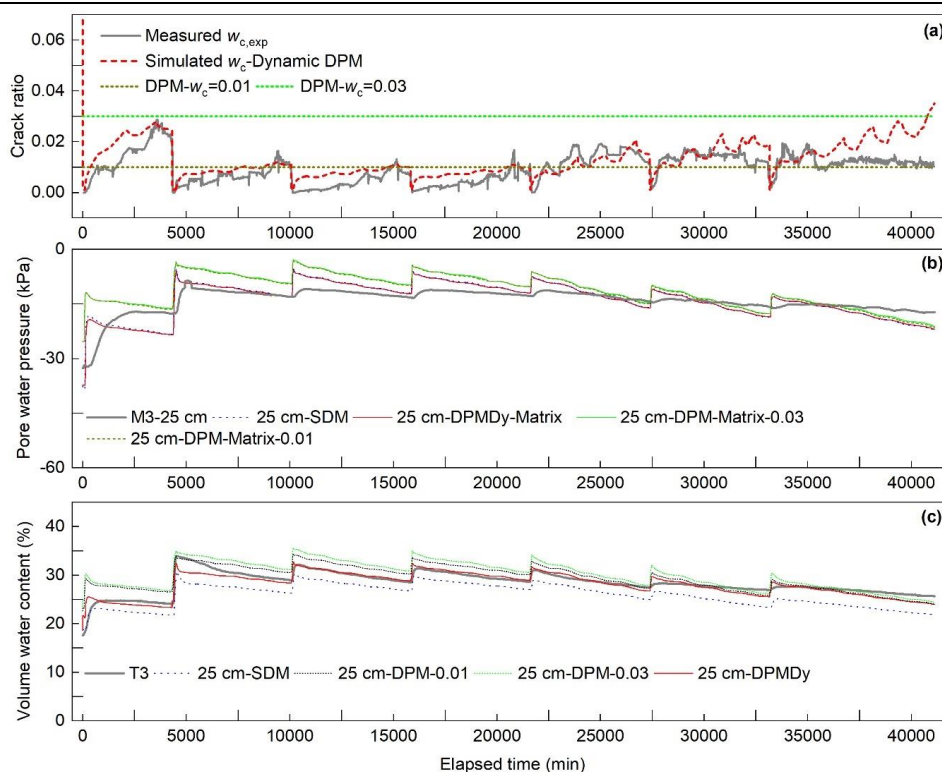
### 478 5.3.3 Crack dynamic changes and hydrological response

479 **Fig. 15** shows part of the comparison results between the measured data and the three models. Detailed descriptions of all the  
 480 comparison results are presented in **Appendix A**. Overall, all models show similar response trends with the measured data.  
 481 Divergences among the three models mainly appeared during drying.

482 In **Fig. 15a**, the simulated surficial  $w_{c,sim}$  was not only generally close to the  $w_{c,exp}$  in value and trend, but also it captured  
 483 the transient slow decrease of  $w_{c,exp}$  during low evaporation periods. Notably, significant overprediction appeared in the 6<sup>th</sup>  
 484 and 7<sup>th</sup> wetting-drying cycles.

485 In **Fig. 15b**, the matric suction ( $S_{sim}$ ) at the 25 cm depth simulated by SDM and DPMDy was close to each other and had an  
 486 average divergence 2.26 kPa to the measured data. The  $S_{sim}$  simulated by DPM had a greater average divergence of 3.4 kPa  
 487 to the measured data. They showed systematic underprediction compared to the  $S_{sim}$  simulated by SDM and DPMDy, but  
 488 their differences became smaller with the increasing WD cycles.

489 In **Fig. 15c**, the total volumetric water content  $\theta_{sim}$  simulated by SDM was much lower with respect to the DPMDy and  
 490 DPM. The  $\theta_{sim}$  simulated by DPM-0.01 and DPM-0.03 overpredicted the volumetric water content. The DPMDy provided  
 491 better prediction results but also showed slight underprediction to the measured data at the last two WD cycles.



492

493 **Fig. 15** Temporal evolution of the measured and simulated crack ratio, matric suction and volumetric water content. (a)  
 494 Measured and simulated crack ratio on soil surface; (b) Measured and simulated matric suction at 25 cm depth; (c) Measured  
 495 and simulated total water content at 25 cm depth

496 **6. Discussions**

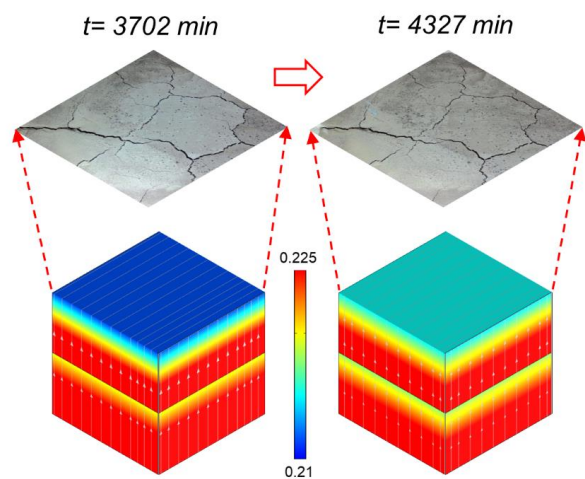
497 6.1 Crack dynamic changes

498 Our experimental results demonstrated that the crack evolution is not always positively correlated to the increase of the WD  
 499 cycles,  $T$  and  $PE$ . For instance, the 5 cm  $\theta_{exp}$  at the end of the final three WD cycles was lower than that in the 1<sup>st</sup> WD cycle  
 500 due to the increased  $T$  and  $PE$ , but the maximum  $w_{c,exp}$  measured during the final three WD cycles was much less than that  
 501 in the 1<sup>st</sup> WD cycle. From the energy-driven perspective, soil cracking and propagation can be regarded as a process that the  
 502 shrinkage energy (or stress), built up from the evaporation and thermal radiation, was released until a critical moment when  
 503 the tensile strength of soil is reached (Peron et al., 2009). If the environmental condition changes in a stable range, the  
 504 desiccation cracks will vary within the crack pattern and the maximum  $w_{j,exp}$  that were formed under the maximum  
 505 shrinkage energy. In this case, new desiccation cracks will not appear in the remained soil matrix during WD cycles (Fig 5b1-  
 506 b4). One reason is that the shrinkage energy can be fully released via previous cracks. The other reason is that the shrinkage  
 507 energy is not high enough to split the soil matrix that has a denser structure (or higher tensile strength) than its initial state  
 508 prior to shrinkage (Luo et al., 2021). However, once the evaporation rate and thermal radiation increase to exceed the stable  
 509 range, higher shrinkage energy will lead to new cracks appearing in the soil matrix that will concurrently restrain the width  
 510 increase of the previous cracks (Wang et al., 2018). This is the reason that cracks in the final three WD cycles are finer than  
 511 the first four WD cycles. Our model describes the crack evolution mainly from the hydrological-driven perspective that  
 512 assumed the surface crack pattern has become stable after undergoing 13 WD cycles and has a constant function relationship  
 513 with the water content. Indeed, this assumption is reasonable for natural soils under atmospheric environmental conditions.  
 514 However, our experiment not only used reconstituted soil but also intensely changed the environmental conditions since the





515 5<sup>th</sup> WD cycle. Therefore, the model overpredicted  $w_{c,exp}$  at the end of the 6<sup>th</sup> and 7<sup>th</sup> WD cycles.  
516 In addition, another interesting phenomenon is the transient decrease of  $w_{c,exp}$  and increase of 5 cm  $\theta_{exp}$  during low  
517 evaporation periods, which we called as ‘self-closure’ process. In light of **Fig 6** and **Fig 8**, the self-closure process appeared  
518 always accompanied by relatively high  $RH$ . From the insight of the experiment, it is natural and common to infer that the  
519 moist air wetted the surface soil from top to bottom, resulting in the self-closure phenomenon. Interestingly, our model does  
520 not incorporate the vapor flow into the boundary conditions, and also the evaporation boundary only involves the outflow of  
521 water, but it still managed to capture the self-closure process. **Fig 16** shows the crack images at  $t = 3702$  and  $4327$  min as  
522 well as the corresponding cloud chart of  $\theta_{sim}$ . It can be seen that the soil surface became moist during the low evaporation  
523 period, which is a typical external phenomenon reflecting the self-closure process. The simulation results show that  $\theta_{sim}$   
524 near the surface soil increased during evaporation while  $\theta_{sim}$  at deep soils decreased, indicative of evaporation inducing the  
525 deep water move up and wet the surface soil from bottom to top. We further found that the process occurred because the water  
526 flow driven by the soil water potential gradients, existing between the wet and dry soil layers, overcame the gravity. Indeed,  
527 this kind of ‘hydraulic lift’ process frequently occurs in planted soils where root zone soil can force water flow from moist  
528 deep soil layers to dry shallow soil layers (Richards and Caldwell, 1987; Bauerle et al., 2008), but was rarely reported in  
529 homogeneous bare soil. We infer that the evaporation boundary conditions using Eq. (14) might play a positive role in leading  
530 water move up and constraining it within the surficial soil depths when the evaporation intensity decreased. In any case, our  
531 results provide an additional possible explanation to the self-closure phenomenon. Further quantitative analysis based on gas-  
532 liquid two phase flow model is needed to compare the contribution of ‘hydraulic lift’ and moist air to the self-closure process  
533 of cracks.



534  
535 **Fig. 16** Self-closure process of cracks captured in experiment (Upper figures) and numerical model (Lower figures) during  
536 the low evaporation process. The left part is at the beginning of the final low evaporation stage during the 1<sup>st</sup> drying periods,  
537 while the right part is at the end of the final low evaporation stage during the 1<sup>st</sup> drying periods.

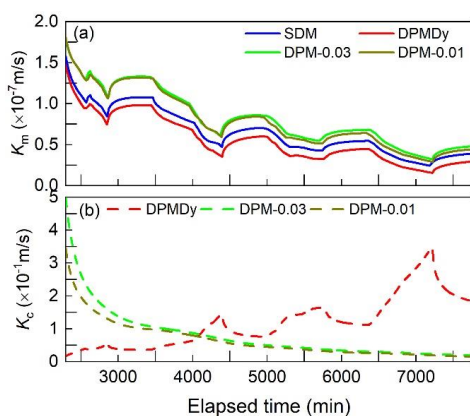
## 539 6.2 Water flow with dynamic changes of desiccation cracks

### 540 6.2.1 Water fluxes

541 As mentioned in section 5.3.1, during the drying process, the matrix and crack evaporation simulated by the DPMDy are  
542 overall lower and higher than other models, respectively. It can be explained by looking at the variation of boundary  $K_m$  and  
543  $K_c$  in each model. Take the time span in **Fig.13a2** as an example, because the DPMDy considers the effects of matrix shrinkage  
544 on the  $K_m$  using Eq. (26), the  $K_{m,DPMDy}$  is always approximately 20% and 30% lower than that of the SDM and DPM,



545 respectively (**Fig. 17a**). On the contrary, because the DPM links the  $K_c$  with the saturation degree of the crack domain (see  
 546 Eq. (25)), the  $K_{c,DPM}$  is destined to decrease with the decreased saturation degree of the crack domain induced by drying, while  
 547 the  $K_{c,DPMDy}$  increases with the crack development induced by drying in light of Eq. (28-b). The ultimate  $K_{c,DPMDy}$  is 80%  
 548 higher than the  $K_{c,DPM}$  (**Fig. 17b**). Indeed, the decrease of  $K_c$  with the drying process is an unrealistic and physically-  
 549 unreasonable results. We can image that after long-term drought, the  $K_{c,DPM}$  will decline to nearly zero according to Fig. 12d,  
 550 which will greatly underestimate the propagation of the PF-DC in the subsequent storm event. However, many laboratory and  
 551 field experiments have observed that heavy rainfall following a long-term drought facilitated PF-DC (Baram et al., 2012a;  
 552 2013; Greve et al., 2010; Kurtzman and Scanlon, 2011; Schlögl et al., 2022). By contrast, the DPMDy has the potential to  
 553 capture this process for its increasing  $K_c$  with the enlarging desiccation crack during the long-term drought. In this study,  
 554 because the experiment scale (or crack volume) is small, the increment of PF-DC simulated by the DPMDy after high-intensity  
 555 evaporation is not significant (despite increment = 25%), but we believe the DPMDy will have a better performance in a  
 556 larger scale (i.e slope scale).



557  
 558 **Fig. 17** Variation of boundary  $K_m$  and  $K_c$  in each model during the 5<sup>th</sup> drying periods. (a)  $K_m$ ; (b)  $K_c$

559

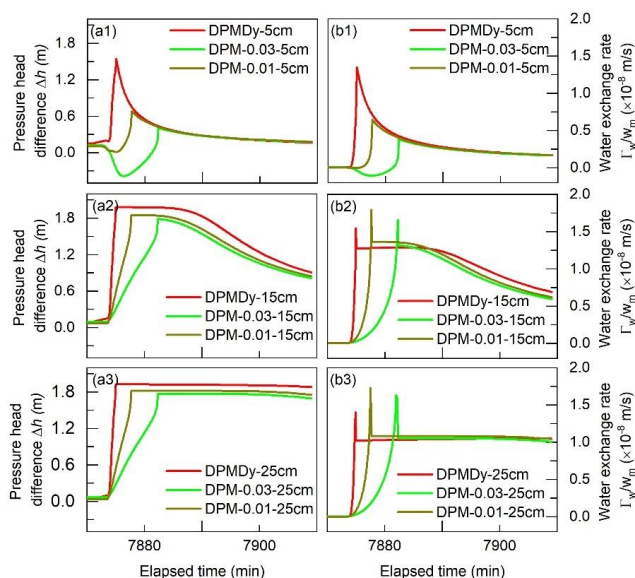
### 560 6.2.2 Water exchange and distribution

561 For the dual-permeability model, the two domains are coupled by the water exchange term (Eq. 3) that is governed by the  
 562 pressure head difference between the two domains ( $\Delta h = h_c - h_m$ ), water exchange coefficient ( $\alpha_w$ ) and the hydraulic  
 563 conductivity between the two domains ( $K_a$ ). The higher the  $\Gamma_w$ , the quicker the two domains equilibrate. Generally, the  
 564 higher  $\Gamma_w$  leads to faster water exchange from the crack domain into the matrix domain and thus boosts the contribution of  
 565 preferential flow on the water distribution in the soil matrix. According to the previous studies, the commonly used magnitude  
 566 of the product of saturated  $\alpha_w K_a$  in clay soils ranges from  $10^{-5} \text{ m}^{-1}\text{s}^{-1}$  (Aguilar - López et al., 2020) to  $10^{-6} \text{ m}^{-1}\text{s}^{-1}$  (Coppola  
 567 et al., 2012; 2015; Gerke and Maximilian Köhne, 2004; Vogel et al., 2000). In this study, the saturated  $\alpha_w K_a$  is  $1.16 \times 10^{-5}$   
 568  $\text{m}^{-1}\text{s}^{-1}$ , which falls in the reasonable range. Building on the above statement, the  $\Delta h$  and water exchange rates ( $\Gamma_w / w_m$ ) for  
 569 both the DPM and DPMDy at the 5 cm, 15 cm and 25 cm depths during the 6<sup>th</sup> rainfall event are graphed in **Fig. 18**.

570 As shown in **Fig. 18a1-a3**,  $\Delta h$  at all depths simulated by both the DPM and DPMDy rapidly reaches a positive peak value  
 571 and gradually decreases with the rainfall process. The rapidly increasing positive value is because the crack domain gets  
 572 saturation earlier than the surrounding soil matrix due to the influx of preferential flow and the small crack storage space in  
 573 this study. The decrease of the  $\Delta h$  is ascribed to the increase of  $h_m$  with water exchanging from crack to matrix domain.



574 Notably, the crack closure process during rainfall process leads to decrease of crack volume (or crack water storage space),  
 575 the ‘water table’ (saturated zone) in the shrinking cracks elevates faster than that in the constant larger crack volume, which  
 576 means the  $h_c$  simulated by DPMDy is higher than the DPM-0.01 and DPM-0.03. Consequently, the time for  $\Delta h$  reaching  
 577 the peak value simulated by the DPMDy is the earliest at all the three depths, then followed by the DPM-0.01 and DPM-0.03.  
 578 The  $\Gamma_w / w_m$  simulated by the DPMDy shows the similar trend to the  $\Delta h$  (**Fig. 18b1-b3**). During the 6<sup>th</sup> rainfall event, its  
 579 cumulative  $\Gamma_w / w_m$  at the 5 cm, 15 cm and 25 cm depths is (26%, 50%), (10%, 26%) and (3%, 14%) larger than that of the  
 580 DPM-0.01 and DPM-0.03, respectively.  
 581 This result means that the crack closure during wetting benefits the building-up process of the pressure head in the crack  
 582 domain and thus can promote water exchange from crack into matrix domain. It corresponds to some experimental results  
 583 that the PF-DC also exists and leads water rapidly infiltrate into soils even desiccation cracks are nearly closed (Baram et al.,  
 584 2012a; Greve et al., 2010; Luo et al., 2021; Sander and Gerke, 2007; Tuong et al., 1996). It also means using DPM may  
 585 overestimate the flux of PF-DC, but underestimate the water exchange coming from the PF-DC. Because the experimental  
 586 scale, crack ratio and depth in this study is small, the difference of simulation result involving the matric suction and water  
 587 content between the DPM and DPMDy is not very significant. However, we can image that the deviation caused by the DPM  
 588 at a larger scale will be more significant, especially in a typical shrinking-swelling soil slope under long-term WD cycles.



589  
 590 **Fig. 18** Pressure head difference (a1-a3) and water exchange rate (b1-b3) between the two domains at the 5 cm, 15 cm and  
 591 25 cm depths during the 6<sup>th</sup> rainfall event. The positive value of water exchange rate is for the water flowing from the crack  
 592 to the matrix domain, while the negative value for the opposite direction

593  
 594 6.3 Model performance

595 In this study, the simulation results show that the DPMDy, which incorporates the dynamic changes of desiccation cracks and  
 596 hydraulic conductivity into the dual-permeability model, has an overall better performance than the SDM and DPM. With  
 597 regard to the water flux, while the three models all have acceptable errors to the measured data, the DPM overpredicted the  
 598 water flux of PF-DC but underestimate the water exchange from cracks to soil matrix. It implies that adopting a constant  
 599 crack volume in the DPM model, whether it is an average or a maximum value of the measured crack ratio, will overestimate  
 600 the PF-DC, which may be unsuitable to evaluate the irrigation efficiency. With regard to the matric suction (or pore water  
 601 pressure), although the SDM has good performance as the DPMDy does, it significantly underpredicted the volume water



602 content and thus may overestimate landslide stability in a moisture-content-dependent threshold method. Further, we expect  
603 that the SDM may show much poorer performance if one applies it to scenarios where the cracks are deeper and the soil has  
604 a higher swelling-shrinking ability than that of our experiment. A comprehensive model sensitivity analysis will be conducted  
605 in our future work.

606 Compared to other dynamic preferential flow models, the DPMDy developed in this study also has its unique advantages.  
607 Firstly, the variation of crack volume (or crack ratio) in our model is deduced from the changes of matrix porosity due to  
608 shrinkage and thus has a physically-consistent as well as a universal definition. Instead, Coppola et al. (2012); (2015) linked  
609 the crack ratio to the suction head with an empirical natural logarithm function, which not only implies a disconnection  
610 between hydrological properties and porosity in the crack domain but also may not be universal when applying it to other  
611 kinds of soils. Secondly, a common defect both in Coppola et al. (2012); (2015) and classical DPM is that they often set the  
612 hydraulic conductivity of the crack domain ( $K_c$ ) varies as a function of the saturated degree calculated from the SWRC of the  
613 crack domain (i.e Eq. (25)). This will lead to an unreasonable extremely low  $K_c$  in drying initial conditions (Aguilar - López  
614 et al., 2020). In our model, we set the relative hydraulic conductivity of the crack domain to unit ( $K_r = 1$ ). It ensures that the  
615 magnitude of  $K_c$  only depends on the crack area or the saturated degree of the soil matrix domain, which provides a potential  
616 solution for remedying the shortcoming mentioned above. Thirdly, compared to some dynamic preferential flow models  
617 neglecting the water exchange between the two domains (Jamalinia et al., 2020; Kroes et al., 2000; Luo et al., 2021; Stewart,  
618 2018) or adopting an improper exchange term (Coppola et al., 2012; 2015), our model tentatively adopts an improved  
619 exchange term proposed by Gerke et al. (2013), which is proved to be a logically correct and satisfactory improvement in  
620 simulating water exchange in our experiment.

621 Because our model neglects the effect of hysteresis both in the soil deformation and soil-water retention curve, it inevitably  
622 caused some errors when compared to the measured water content, especially for the surficial soil layer that has been  
623 significantly affected by the WD cycles. Our future work will try to incorporate the hysteresis effect into the current model to  
624 further improve the prediction strength. Besides, we have to remind again that because the shrinking-swelling model in our  
625 method is developed based on the hydrological-driven perspective, it may be more suitable in the natural soil layer where the  
626 crack pattern has a stable state after long-term WD cycles.

## 627 7. Conclusions

628 This study combined an experimental study and a numerical simulation to quantify the preferential flow induced by dynamic  
629 changes of desiccation cracks (PF-DC). A soil column infiltration test under wetting-drying conditions was conducted to  
630 investigate dynamic changes of desiccation cracks and the accompanying water infiltration process. The variation of crack  
631 geometry, including crack ratio, width and depth were measured. The soil volumetric water content, matric suction and water  
632 drainage were also monitored. A new dynamic dual-permeability model (DPMDy) was developed to account for the PF-DC,  
633 which includes physically-consistent functions in describing the variation of both porosity and hydraulic conductivity in crack  
634 and matrix domains. The performance of the single-domain model (SDM), rigid dual-permeability model (DPM) and DPMDy  
635 was evaluated by comparing their simulation results to the monitoring data.

636 Overall, the DPMDy performed not only better prediction on the crack evolution and hydrological response with respect to  
637 the SDM and DPM, but also provided much better descriptions on the underlying physics involving the PF-DC. During the  
638 drying periods, the matrix evaporation modeled by the DPMDy is lower than that of the SDM and DPM due to considering  
639 the permeability decay induced by soil shrinkage. But the crack evaporation modelled in the DPMDy approach is the highest  
640 because it managed to capture the raised crack permeability induced by drying-enlarging desiccation cracks. Compared to the  
641 DPM with fixed crack volume, the DPMDy revealed that the crack closure process during wetting will lead to a faster pressure  
642 head building-up process in the crack domain and higher water exchange rates from the crack to the matrix domain.



643 Additionally, using a fixed crack ratio in the DPM, whether it is the maximum or the average value from the experiment data,  
644 will overestimate the infiltration fluxes of PF-DC but underestimate its contribution to the matrix domain.  
645 The DPMDy developed here has a physically-consistent definition. It remedies the shortcomings of the RDPM and other  
646 dynamic preferential flow models in defining the dynamic changes of desiccation cracks and hydraulic properties of the crack  
647 domain and interface. Future works should focus on considering the hysteresis effect of the SWRC curve during wetting-  
648 drying cycles in the model and its application to complex field situations.

649

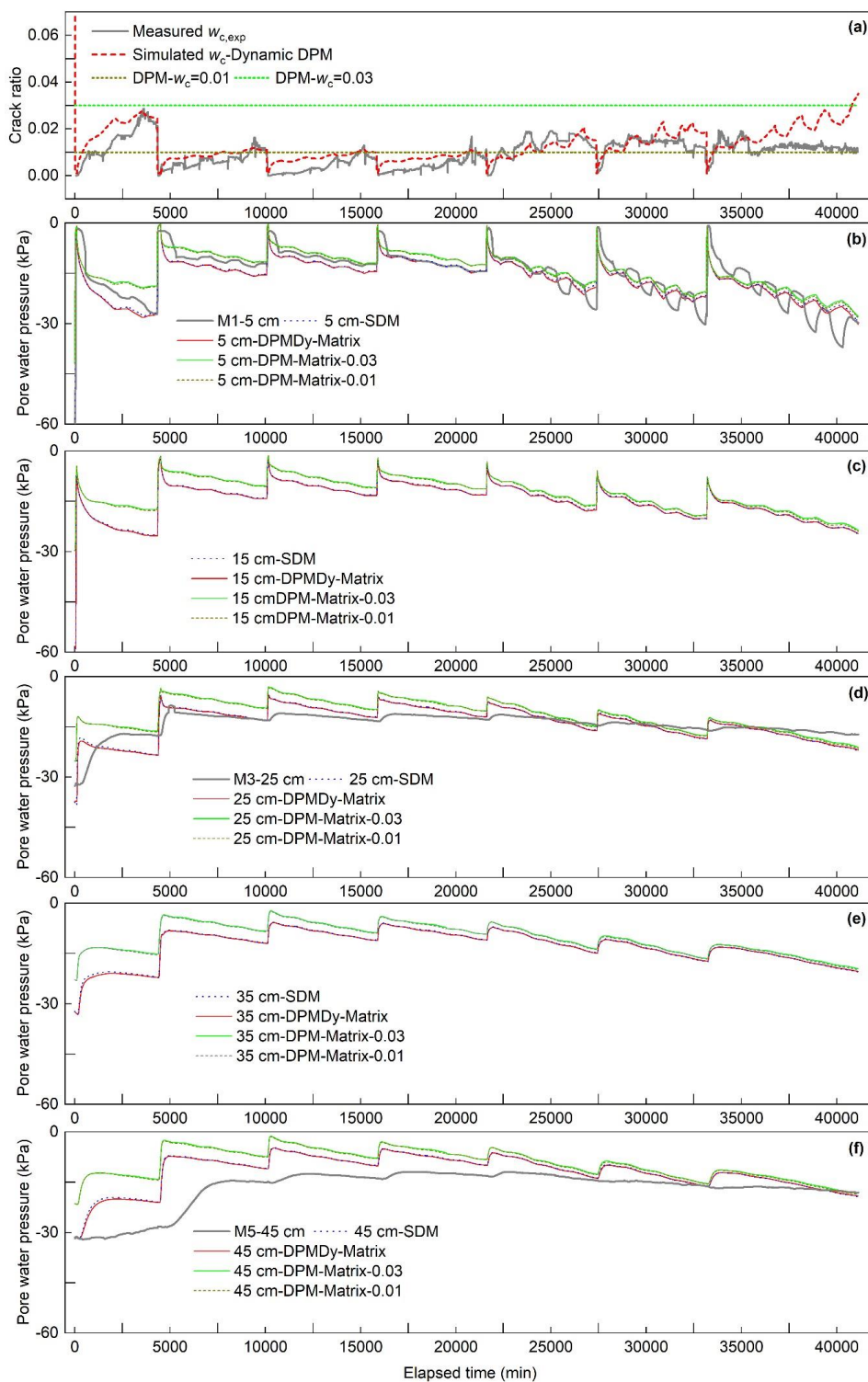
#### 650 Appendix A

651 **Fig. A1** and **Fig. A2** show the temporal evolution of the measured and simulated crack ratio on the soil surface, matric suction  
652 (negative pore water pressure) and volumetric water contents at the five monitoring depths (5, 15, 25, 35 and 45 cm).

653 In **Fig A1a**, the simulated  $w_{c,sim}$  was not only generally close to the  $w_{c,exp}$  in value and trend, but also it captured the  
654 transient slow decrease of  $w_{c,exp}$  during low evaporation periods.

655 In **Fig A1b-f**, the matric suction ( $S_{sim}$ ) simulated by SDM and DPMDy is close to each other and has average divergence of  
656 2.75 kPa, 2.26 kPa and 5.02kPa to the measured data at the 5 cm, 25 cm and 45 cm depths, respectively. The  $S_{sim}$  simulated  
657 by DPM has a greater average divergence of 2.78 kPa, 3.4 kPa and 7.43 kPa to the measured data at the three corresponding  
658 depths.

659 In **Fig A2a-e**, the volumetric water content  $\theta_{sim}$  simulated by SDM was much lower than that simulated by DPMDy and  
660 DPM. In most depths (except the 5 cm and 45 cm depth), SDM systematically underpredicted the volumetric water content  
661 during both wetting and drying periods. By contrast, the  $\theta_{sim}$  simulated by DPM-0.01 and DPM-0.03 overpredicted the  
662 volumetric water content. The DPMDy gave overall better prediction results in most depths, but has significant divergences  
663 to the measured data at the depth of 5 cm and so are the other two models.



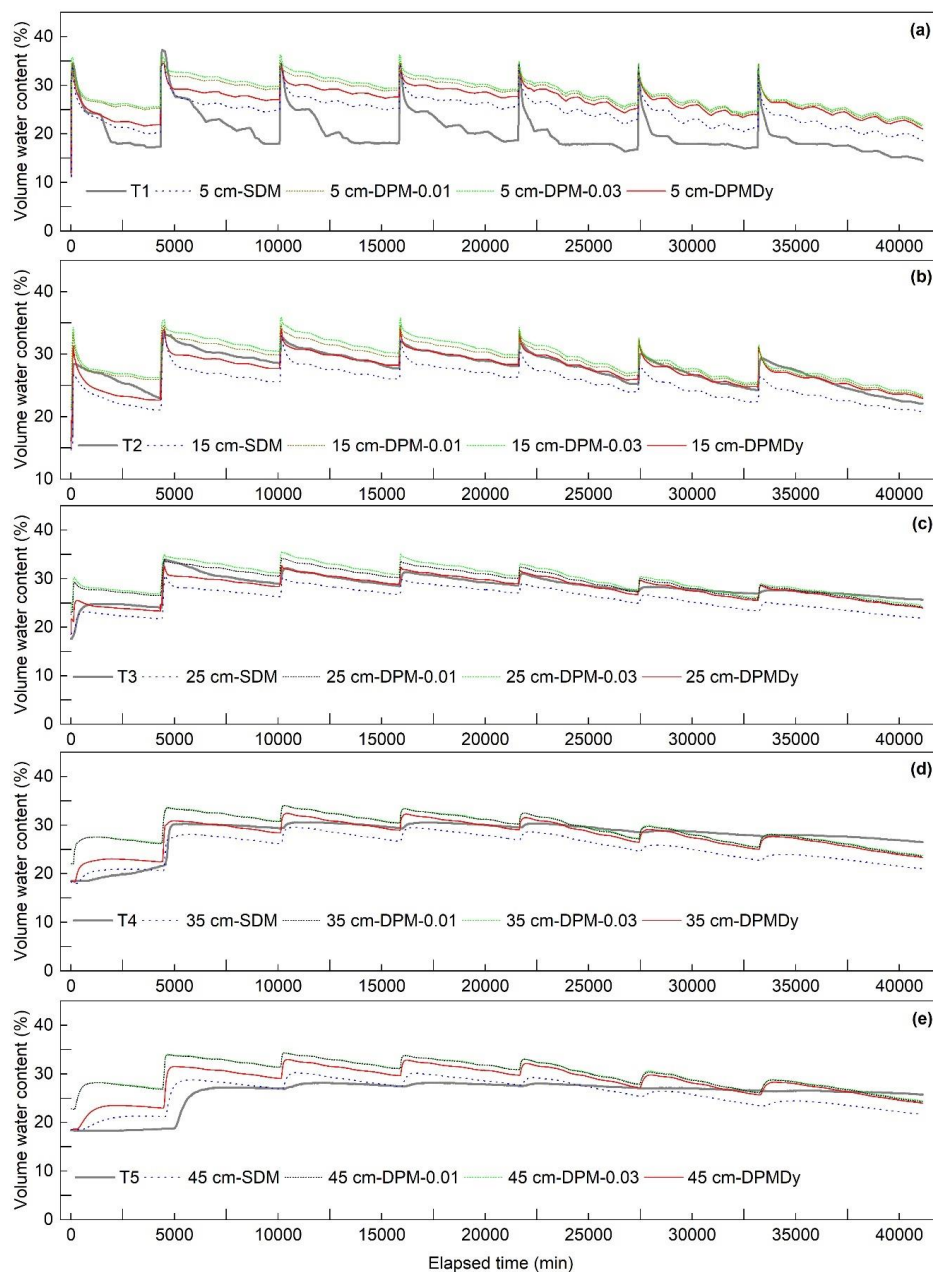
664

665 **Fig. A1** Temporal evolution of the measured and simulated crack ratio and matric suction at different depths. (a) Measured

666 and simulated crack ratio (Dynamic DPM) on soil surface; (b-f) Measured and simulated matric suction (Single domain model,

667 DPM and Dynamic DPM) at depths of 5 cm, 15 cm, 25 cm, 35 cm and 45 cm.





668  
 669 **Fig. A2** Temporal evolution of the measured and simulated volumetric water content at depths of 5 cm, 15 cm, 25 cm, 35 cm  
 670 and 45 cm. Note that the simulated volumetric water content demonstrated here is the total volumetric water content that  
 671 combined with the combined matrix and crack domains using Eq. (8)

672 **Notation**

PF-DC	Preferential flow induced by desiccation cracks
SDM	Single-domain model
EMs	Explicit crack models
DPoM	Dual-porosity model
DPM	Rigid dual-permeability model with fixed crack ratio and hydraulic conductivity



DPM-0.01	Rigid dual-permeability model with crack ratio of 0.01
DPM-0.03	Rigid dual-permeability model with crack ratio of 0.03
DPMDy	Dynamic DPM with changing crack ratio and hydraulic conductivity
WD cycles	Wetting-drying cycles
$\theta$	Total water content (combined matrix and crack domains), $\text{m}^3\text{m}^{-3}$
$\theta_{\text{exp}}$	Volumetric water content measured in the experiment, $\text{m}^3\text{m}^{-3}$
$\theta_m$	Volumetric water content of the matrix domain, $\text{m}^3\text{m}^{-3}$
$\theta_c$	Volumetric water content of the crack domain, $\text{m}^3\text{m}^{-3}$
$\theta_{m,s}$	Saturated volumetric water content of the matrix domain, $\text{m}^3\text{m}^{-3}$
$\theta_{m,r}$	Residual volumetric water content of the matrix domain, $\text{m}^3\text{m}^{-3}$
$\theta_{c,s}$	Saturated volumetric water content of the crack domain, $\text{m}^3\text{m}^{-3}$
$\theta_{c,r}$	Residual volumetric water content of the crack domain, $\text{m}^3\text{m}^{-3}$
$S_{e,m}$	Saturation degree of the matrix domain, $\text{m}^3\text{m}^{-3}$
$S_{e,c}$	Saturation degree of the crack domain, $\text{m}^3\text{m}^{-3}$
$\alpha_m$	Parameter for the van Genuchten water retention curve of the matrix domain, 1/m
$n_m$	Parameter for the van Genuchten water retention curve of the matrix domain, 1/m
$m_m$	Parameter for the van Genuchten water retention curve of the matrix domain, 1/m
$\alpha_c$	Parameter for the van Genuchten water retention curve of the crack domain, 1/m
$n_c$	Parameter for the van Genuchten water retention curve of the crack domain, 1/m
$m_c$	Parameter for the van Genuchten water retention curve of the crack domain, 1/m
$h_m$	Pressure head of the matrix domain, m
$h_c$	Pressure head of the crack domain, m
$C_c$	Specific water capacity of the crack domain which is defined as $d\theta_c / dh_c$ , 1/m
$C_m$	Specific water capacity of the matrix domain which is defined as $d\theta_m / dh_m$ , 1/m
$K_s$	Total transient saturated hydraulic conductivity of the soil (combined matrix and crack domains), m/s
$K_c$	Transient hydraulic conductivity of the crack domain, m/s
$K_{c,s}$	Saturated hydraulic conductivity of the crack domain, m/s
$K_{c,\text{max}}$	The maximum crack hydraulic conductivity when the crack reaches its maximum crack aperture, m/s
$K_{c,\text{min}}$	The minimum crack hydraulic conductivity when the crack reaches its minimum crack aperture, m/s
$K_{c,r}$	Relative hydraulic conductivity of the crack domain, $\text{m}^3\text{m}^{-3}$
$K_m$	Transient hydraulic conductivity of the matrix domain, m/s
$K_{m,s}$	Saturated hydraulic conductivity of the matrix domain, m/s
$K_{m,\text{max}}$	The maximum matrix hydraulic conductivity prior to soil shrinkage, m/s
$K_{m,r}$	Relative hydraulic conductivity of the matrix domain, $\text{m}^3\text{m}^{-3}$
$K_a$	Hydraulic conductivity between the matrix and crack domains, m/s
$K_{a,\text{min}}$	An improved hydraulic conductivity between the matrix and crack domains reformulated by Gerke et al. (2013), m/s
$\Gamma_w$	Water exchange term between the crack and matrix domains, 1/s
$w_c$	Crack ratio, which is defined as volumetric ratio between the crack domain and the overall soil volume, $\text{m}^3\text{m}^{-3}$
$w_{c,\text{exp}}$	Surface crack ratio measured in experiment, $\text{m}^2\text{m}^{-2}$
$w_{j,\text{exp}}$	Average crack aperture (or crack width) measured in the experiment, m
$w_{j,\text{max}}$	The maximum average crack aperture measured in the experiment, m
$d_{\text{max}}$	The maximum crack depth measured in the experiment, m
$w_m$	Volumetric ratio between the matrix domain and the overall soil volume, $\text{m}^3\text{m}^{-3}$



$\alpha_w$	Effective water transfer coefficient, $1/m^2$
$V$	Total soil volume (combined matrix and crack domains), $m^3$
$V_m$	Volume of the soil matrix domain, $m^3$
$V_c$	Volume of the crack domain, $m^3$
$V_p$	Total pore volume, $m^3$
$V_{p,m}$	Pore volume in the matrix domain, $m^3$
$V_{p,c}$	Pore volume in the crack domain, $m^3$
$\varepsilon$	Total soil porosity (combined matrix and crack domains), which is defined as $V_p/V$ , $m^3m^{-3}$
$\varepsilon_m$	Effective porosity of the matrix domain, which is defined as $V_{p,m}/V_m$
$\varepsilon_c$	Effective porosity of the crack domain, which is defined as $V_{p,c}/V_c$
$i$	Total effective infiltration rate (combined matrix and crack domains), $m/s$
$i_m$	Effective infiltration rate of the matrix domain, $m/s$
$i_c$	Effective infiltration rate of the crack domain, $m/s$
$e_m$	Effective evaporation rate of the matrix domain, $m/s$
$e_c$	Effective evaporation rate of the crack domain, $m/s$
$r$	Rainfall intensity, $m/s$
$AE$	Actual evaporation rate, $m/s$
$PE$	Potential evaporation rate, $m/s$
$S$	Total matric suction at the soil surface, $kPa$
$S_{exp}$	Soil matric suction measured in the experiment, $kPa$
$g$	Gravitational acceleration constant, $m/s^2$
$\omega_w$	Molecular mass of water, $kg/mol$
$\xi$	Dimensional empirical parameter with a suggested value of 0.7
$h_a$	Relative humidity of soil overlying air
$\gamma_w$	Unit mass of water, $kN/m^3$
$R$	Universal gas constant, $J/mol \cdot K$
$T_s$	Soil surface temperature, $^{\circ}C$
$\phi_{max}$	Total porosity (or the maximum porosity) of a soil core prior to soil shrinkage, which is defined as $V_p/V$ and thus equals to the $\varepsilon$ , $m^3m^{-3}$
$\phi_{min}$	The minimum porosity of the matrix domain, $m^3m^{-3}$
$\phi_{matrix}$	Porosity of the matrix domain, which is defined as $V_{p,m}/V$ , $m^3m^{-3}$
$\phi_{crack}$	Porosity of the crack domain, which is defined as $V_{p,c}/(V_m+V_c)$ , $m^3m^{-3}$
$\phi_{sub}$	Porosity of the subsidence zone, which is defined as voids induced by soil subsidence divided by the total soil volume, $m^3m^{-3}$
$U$	A unified water content, which is defined as the gravimetric water content $u$ divided by its saturated value $u_{max}$
$p$	Functional shape parameters of the soil shrinkage curve
$q$	Functional shape parameters of the soil shrinkage curve
$\nu$	Water kinematic viscosity, $m^2/s$
$t_p$	Beginning of ponding time after each rainfall, $min$
$\Delta h$	Pressure difference between the crack and matrix domains, which is defined as $h_c - h_m$

673

674 **Code/Data availability**

675 The source code and the data generated from this study are available from the corresponding author upon reasonable request.

676

677 **Author contribution**



---

678 Yi Luo: Conceptualization, Methodology, Investigation, Writing-original draft preparation

679 Jiaming Zhang\*: Supervision, Writing - review & editing, Project administration

680 Zhi Zhou: Resources, Software, Investigation

681 Juan P. Aguilar-Lopez: Writing - review & editing

682 Roberto Greco: Writing - review & editing

683 Thom Bogaard: Supervision, Writing - review & editing, Funding acquisition

684

#### 685 **Competing interests**

686 Some authors are members of the editorial board of journal Hydrology and Earth System Sciences. The peer-review process  
687 was guided by an independent editor, and the authors have also no other competing interests to declare.

688

#### 689 **Financial support**

690 This work was financially supported by the National Natural Science Foundation of China (42177166) and the Fundamental  
691 Research Funds for National University, China University of Geosciences (Wuhan). It was also partially funded by the Plan  
692 of Anhui Province Transport Technology Progress (grant 2018030) and Engineering Research Center of Rock-Soil Drilling  
693 & Excavation and Protection, Ministry of Education (202210).

694

#### 695 **Acknowledgment**

696 This paper was written during visiting research exchange of Yi Luo at TUDelft in Summer 2022. The experiment was  
697 conducted from January to March 2022 in China, Professor Ming-jian Hu and his research group are thanked for their great  
698 help in providing TDR probes. Yi Luo's Chinese colleagues Yuhao Li, Zhan Yang, Xiang Li, Zijian Shen are thanked for their  
699 contribution on the experiment monitoring. The authors also would like to thank the editor and anonymous reviewers for their  
700 valuable comments that substantially improved this paper.

701



---

## 702 References

- 703 Aguilar-López, J. P., Bogaard, T. A., and Gerke, H. H.: Dual-Permeability Model Improvements for Representation of Preferential  
704 Flow in Fractured Clays, *Water Resour. Res.*, 56, 10.1029/2020wr027304, 2020.
- 705 Arora, B., Mohanty, B. P., and McGuire, J. T.: Inverse estimation of parameters for multidomain flow models in soil columns with  
706 different macropore densities, *Water Resour. Res.*, 47, 2010WR009451, 10.1029/2010WR009451, 2011.
- 707 Baram, S., Kurtzman, D., and Dahan, O.: Water percolation through a clayey vadose zone, *J. Hydrol.*, 424-425, 165-171,  
708 10.1016/j.jhydrol.2011.12.040, 2012a.
- 709 Baram, S., Ronen, Z., Kurtzman, D., Külls, C., and Dahan, O.: Desiccation-crack-induced salinization in deep clay sediment, *Hydrol.*  
710 *Earth Syst. Sci.*, 17, 1533-1545, 10.5194/hess-17-1533-2013, 2013.
- 711 Bauerle, T. L., Richards, J. H., Smart, D. R., and Eissenstat, D. M.: Importance of internal hydraulic redistribution for prolonging  
712 the lifespan of roots in dry soil, *Plant Cell Environ.*, 31, 177-186, 10.1111/j.1365-3040.2007.01749.x, 2008.
- 713 Bogaard, T. A. and Greco, R.: Landslide hydrology: from hydrology to pore pressure, *WIREs Water*, 3, 439-459, 10.1002/wat2.1126,  
714 2015.
- 715 Caris, J. P. T. and Van Asch, T. W. J.: Geophysical, geotechnical and hydrological investigations of a small landslide in the French  
716 Alps, *Eng. Geol.*, 31, 249-276, 10.1016/0013-7952(1)90011-9, 1991.
- 717 Chaduvula, U., Viswanadham, B. V. S., and Kodikara, J.: Centrifuge model studies on desiccation cracking behaviour of fiber-  
718 reinforced expansive clay, *Geotext. Geomembr.*, 50, 480-497, 10.1016/j.geotextmem.2022.02.001, 2022.
- 719 Chen, C., Roseberg, R. J., and Selker, J. S.: Using microsprinkler irrigation to reduce leaching in a shrink/swell clay soil, *Agric.*  
720 *Water Manage.*, 54, 159-171, 10.1016/s0378-3774(01)00150-0, 2002.
- 721 Cheng, Q., Tang, C.-S., Xu, D., Zeng, H., and Shi, B.: Water infiltration in a cracked soil considering effect of drying-wetting cycles,  
722 *J. Hydrol.*, 593, 10.1016/j.jhydrol.2020.125640, 2021.
- 723 Chui, T. F. M. and Freyberg, D. L.: Implementing Hydrologic Boundary Conditions in a Multiphysics Model, *J. Hydrol. Eng.*, 14,  
724 1374-1377, 10.1061/(asce)he.1943-5584.0000113, 2009.
- 725 Coppola, A., Comegna, A., Dragonetti, G., Gerke, H. H., and Basile, A.: Simulated Preferential Water Flow and Solute Transport in  
726 Shrinking Soils, *Vadose Zone J.*, 14, 10.2136/vzj2015.02.0021, 2015.
- 727 Coppola, A., Gerke, H. H., Comegna, A., Basile, A., and Comegna, V.: Dual-permeability model for flow in shrinking soil with  
728 dominant horizontal deformation, *Water Resour. Res.*, 48, 10.1029/2011wr011376, 2012.
- 729 Davidson, M. R.: A Green-Ampt Model of infiltration in a cracked soil, *Water Resour. Res.*, 20, 1685-1690,  
730 10.1029/WR020i011p01685, 1984.
- 731 Dusek, J., Gerke, H. H., and Vogel, T.: Surface Boundary Conditions in Two-Dimensional Dual-Permeability Modeling of Tile Drain  
732 Bromide Leaching, *Vadose Zone J.*, 7, 1287-1301, 10.2136/vzj2007.0175, 2008.
- 733 Favre, F., Boivin, P., and Wopereis, M. C. S.: Water movement and soil swelling in a dry, cracked Vertisol, *Geoderma*, 78, 113-123,  
734 10.1016/s0016-7061(97)00030-x, 1997.
- 735 Gerke, H. H. and Maximilian Köhne, J.: Dual-permeability modeling of preferential bromide leaching from a tile-drained glacial  
736 till agricultural field, *J. Hydrol.*, 289, 239-257, 10.1016/j.jhydrol.2003.11.019, 2004.
- 737 Gerke, H. H. and van Genuchten, M. T.: A dual-porosity model for simulating the preferential movement of water and solutes in  
738 structured porous media, *Water Resour. Res.*, 29, 305-319, 10.1029/92wr02339, 1993a.
- 739 Gerke, H. H. and van Genuchten, M. T.: Evaluation of a first-order water transfer term for variably saturated dual-porosity flow  
740 models, *Water Resour. Res.*, 29, 1225-1238, 10.1029/92wr02467, 1993b.
- 741 Gerke, H. H., Dusek, J., and Vogel, T.: Solute Mass Transfer Effects in Two-Dimensional Dual-Permeability Modeling of Bromide  
742 Leaching From a Tile-Drained Field, *Vadose Zone J.*, 12, 10.2136/vzj2012.0091, 2013.
- 743 Germann, P. F. and Karlen, M.: Viscous-Flow Approach to In Situ Infiltration and In Vitro Saturated Hydraulic Conductivity  
744 Determination, *Vadose Zone J.*, 15, 10.2136/vzj2015.05.0065, 2016.
- 745 Greco, R.: Preferential flow in macroporous swelling soil with internal catchment: model development and applications, *J. Hydrol.*,  
746 269, 150-168, 10.1016/s0022-1694(02)00215-9, 2002.



- 747 Greve, A., Andersen, M. S., and Acworth, R. I.: Investigations of soil cracking and preferential flow in a weighing lysimeter filled  
748 with cracking clay soil, *J. Hydrol.*, 393, 105-113, 10.1016/j.jhydrol.2010.03.007, 2010.
- 749 Hendrickx, J. M. H. and Flury, M.: Conceptual Models of Flow and Transport in the Fractured Vadose Zone, in: Panel on Conceptual  
750 Models of Flow and Transport in the Fractured Vadose Zone, National Academy Press, Washington D.C., 149-187, 2001.
- 751 Jamalnia, E., Vardon, P. J., and Steele-Dunne, S. C.: The impact of evaporation induced cracks and precipitation on temporal slope  
752 stability, *Comput. Geotech.*, 122, 10.1016/j.compgeo.2020.103506, 2020.
- 753 Jarvis, N., Koestel, J., and Larsbo, M.: Understanding Preferential Flow in the Vadose Zone: Recent Advances and Future Prospects,  
754 *Vadose Zone J.*, 15, 10.2136/vzj2016.09.0075, 2016.
- 755 Khan, M. S., Hossain, S., Ahmed, A., and Faysal, M.: Investigation of a shallow slope failure on expansive clay in Texas, *Eng. Geol.*,  
756 219, 118-129, 10.1016/j.enggeo.2016.10.004, 2017.
- 757 Krisnanto, S., Rahardjo, H., Fredlund, D. G., and Leong, E. C.: Water content of soil matrix during lateral water flow through  
758 cracked soil, *Eng. Geol.*, 210, 168-179, 10.1016/j.enggeo.2016.06.012, 2016.
- 759 Kroes, J. G., Wesseling, J. G., and Van Dam, J. C.: Integrated modelling of the soil – water – atmosphere – plantsystem using  
760 the model SWAP 2.0 an overview of theory and application, *Hydrol. Processes*, 14, 10, [https://doi.org/10.1002/1099-1085\(20000815/30\)14:11/12<1993::AID-HYP50>3.0.CO;2-%23](https://doi.org/10.1002/1099-1085(20000815/30)14:11/12<1993::AID-HYP50>3.0.CO;2-%23), 2000.
- 762 Kurtzman, D. and Scanlon, B. R.: Groundwater Recharge through Vertisols: Irrigated Cropland vs. Natural Land, Israel, *Vadose*  
763 *Zone J.*, 10, 662-674, 10.2136/vzj2010.0109, 2011.
- 764 Laine-Kaulio, H., Backnäs, S., Karvonen, T., Koivusalo, H., and McDonnell, J. J.: Lateral subsurface stormflow and solute transport  
765 in a forested hillslope: A combined measurement and modeling approach, *Water Resour. Res.*, 50, 8159-8178,  
766 10.1002/2014wr015381, 2014.
- 767 Larsbo, M. and Jarvis, N. J.: MACRO5.0. A model of water flow and solute transport in macroporous soil. Technical description,  
768 2003.
- 769 Lepore, B. J., Morgan, C. L. S., Norman, J. M., and Molling, C. C.: A Mesopore and Matrix infiltration model based on soil structure,  
770 *Geoderma*, 152, 301-313, 10.1016/j.geoderma.2009.06.016, 2009.
- 771 Liu, C.-W., Cheng, S.-W., Yu, W.-S., and Chen, S.-K.: Water infiltration rate in cracked paddy soil, *Geoderma*, 117, 169-181,  
772 10.1016/s0016-7061(03)00165-4, 2003.
- 773 Luo, Y., Zhang, J.-m., Zhou, Z., Shen, Z.-j., Chong, L., and Victor, C.: Investigation and prediction of water infiltration process in  
774 cracked soils based on a full-scale model test, *Geoderma*, 400, 10.1016/j.geoderma.2021.115111, 2021.
- 775 Mooney, S. J. and Morris, C.: A morphological approach to understanding preferential flow using image analysis with dye tracers  
776 and X-ray Computed Tomography, *Catena*, 73, 204-211, 10.1016/j.catena.2007.09.003, 2008.
- 777 Mualem, Y.: A new model for predicting the hydraulic conductivity of unsaturated porous media, *Water Resour. Res.*, 12, 513-522,  
778 10.1029/WR012i003p00513, 1976.
- 779 Nimmo, J. R.: Theory for Source-Responsive and Free-Surface Film Modeling of Unsaturated Flow, *Vadose Zone J.*, 9, 295-306,  
780 10.2136/vzj2009.0085, 2010.
- 781 Nimmo, J. R., Perkins, K. S., Plampin, M. R., Walvoord, M. A., Ebel, B. A., and Mirus, B. B.: Rapid-Response Unsaturated Zone  
782 Hydrology: Small-Scale Data, Small-Scale Theory, Big Problems, *Front. Earth Sci.*, 9, 10.3389/feart.2021.613564, 2021.
- 783 Pei, P., Zhao, Y., Ni, P., and Mei, G.: A protective measure for expansive soil slopes based on moisture content control, *Eng. Geol.*,  
784 269, 10.1016/j.enggeo.2020.105527, 2020.
- 785 Peron, H., Hueckel, T., Laloui, L., and Hu, L. B.: Fundamentals of desiccation cracking of fine-grained soils: experimental  
786 characterisation and mechanisms identification, *Canadian Geotechnical Journal*, 46, 1177-1201, 10.1139/t09-054, 2009.
- 787 Richards, J. H. and Caldwell, M. M.: Hydraulic lift: Substantial nocturnal water transport between soil layers by *Artemisia tridentata*  
788 roots, *Oecologia*, 73, 486-489, 10.1007/BF00379405, 1987.
- 789 Sander, T. and Gerke, H. H.: Preferential Flow Patterns in Paddy Fields Using a Dye Tracer, *Vadose Zone J.*, 6, 105-115,  
790 10.2136/vzj2006.0035, 2007.
- 791 Schlägl, J., Wimmer, B., Cramaro, L., Wirsching, J., Poll, C., Pagel, H., Kandeler, E., Huhn, C., Griebler, C., Stumpp, C., and  
792 Haderlein, S. B.: Heavy rainfall following a summer drought stimulates soil redox dynamics and facilitates rapid and deep





- 793 translocation of glyphosate in floodplain soils, *Environ Sci Process Impacts*, 24, 825-838, 10.1039/d1em00527h, 2022.
- 794 Shao, W., Bogaard, T. A., Bakker, M., and Greco, R.: Quantification of the influence of preferential flow on slope stability using a  
795 numerical modelling approach, *Hydrol. Earth Syst. Sci.*, 19, 2197-2212, 10.5194/hess-19-2197-2015, 2015.
- 796 Šimůnek, J., Jarvis, N. J., van Genuchten, M. T., and Gärdenäs, A.: Review and comparison of models for describing non-equilibrium  
797 and preferential flow and transport in the vadose zone, *J. Hydrol.*, 272, 14-35, 10.1016/s0022-1694(02)00252-4, 2003.
- 798 Smith, R. J., Raine, S. R., and Minkevich, J.: Irrigation application efficiency and deep drainage potential under surface irrigated  
799 cotton, *Agric. Water Manage.*, 71, 117-130, 10.1016/j.agwat.2004.07.008, 2005.
- 800 SNOW, D. T.: A parallel plate model of fractured permeable media, University of California, Berkeley ProQuest Dissertations  
801 Publishing 1965.
- 802 Song, L., Li, J., Garg, A., and Mei, G.: Experimental study on water exchange between crack and clay matrix, *Geomech. Eng.*, 14,  
803 9, <https://doi.org/10.12989/gae.2018.14.3.283>, 2018.
- 804 Stewart, R. D.: A Dynamic Multidomain Green-Ampt Infiltration Model, *Water Resour. Res.*, 54, 6844-6859,  
805 10.1029/2018wr023297, 2018.
- 806 Stewart, R. D.: A Generalized Analytical Solution for Preferential Infiltration and Wetting, *Vadose Zone J.*, 18, 1-10,  
807 10.2136/vzj2018.08.0148, 2019.
- 808 Stewart, R. D., Abou Najm, M. R., Rupp, D. E., and Selker, J. S.: Modeling multidomain hydraulic properties of shrink-swell soils,  
809 *Water Resour. Res.*, 52, 7911-7930, 10.1002/2016wr019336, 2016b.
- 810 Stewart, R. D., Rupp, D. E., Abou Najm, M. R., and Selker, J. S.: A Unified Model for Soil Shrinkage, Subsidence, and Cracking,  
811 *Vadose Zone J.*, 15, 1-15, 10.2136/vzj2015.11.0146, 2016a.
- 812 Tichavsky, R., Ballesteros-Canovas, J. A., Silhan, K., Tolasz, R., and Stoffel, M.: Dry Spells and Extreme Precipitation are The  
813 Main Trigger of Landslides in Central Europe, *Sci Rep*, 9, 14560, 10.1038/s41598-019-51148-2, 2019.
- 814 Tuong, T. P., Cabangon, R. J., and Wopereis, M. C. S.: Quantifying Flow Processes during Land Soaking of Cracked Rice Soils,  
815 *Soil Sci. Soc. Am. J.*, 60, 872-879, 10.2136/sssaj1996.03615995006000030028x, 1996.
- 816 van Genuchten, M. T.: A Closed-form Equation for Predicting the Hydraulic Conductivity of Unsaturated Soils, *Soil Sci. Soc. Am.*  
817 *J.*, 44, 892-898, 10.2136/sssaj1980.03615995004400050002x, 1980.
- 818 van Genuchten, M. T. and Wierenga, P. J.: Mass Transfer Studies in Sorbing Porous Media I. Analytical Solutions, *Soil Sci. Soc.*  
819 *Am. J.*, 40, 473-480, 10.2136/sssaj1976.03615995004000040011x, 1976.
- 820 Vervoort, R. W., Silburn, M., and Kirby, M.: Near surface water balance in the Northern Murray-Darling Basin, *Water Sci. Technol.*,  
821 48, 207-214, 10.2166/wst.2003.0442, 2003.
- 822 Vogel, T., Gerke, H. H., Zhang, R., and Van Genuchten, M. T.: Modeling flow and transport in a two-dimensional dual-permeability  
823 system with spatially variable hydraulic properties, *J. Hydrol.*, 238, 78-89, 10.1016/s0022-1694(00)00327-9, 2000.
- 824 Wang, C., Zhang, Z.-y., Fan, S.-m., Mwiya, R., and Xie, M.-x.: Effects of straw incorporation on desiccation cracking patterns and  
825 horizontal flow in cracked clay loam, *Soil Tillage Res.*, 182, 130-143, 10.1016/j.still.2018.04.006, 2018.
- 826 Wang, Z., Liu, J., Hamoud, Y. A., Wang, Y., Qiu, R., Agathokleous, E., Hong, C., and Shaghaleh, H.: Natural (15)N abundance as  
827 an indicator of nitrogen utilization efficiency in rice under alternate wetting and drying irrigation in soils with high clay contents,  
828 *Sci Total Environ*, 838, 156528, 10.1016/j.scitotenv.2022.156528, 2022.
- 829 Weiler, M.: An infiltration model based on flow variability in macropores: development, sensitivity analysis and applications, *J.*  
830 *Hydrol.*, 310, 294-315, 10.1016/j.jhydrol.2005.01.010, 2005.
- 831 Wen, T., Wang, P., Shao, L., and Guo, X.: Experimental investigations of soil shrinkage characteristics and their effects on the soil  
832 water characteristic curve, *Eng. Geol.*, 284, 10.1016/j.enggeo.2021.106035, 2021.
- 833 Wilson, G. W., Fredlund, D. G., and Barbour, S. L.: The effect of soil suction on evaporative fluxes from soil surfaces, *Canadian*  
834 *Geotechnical Journal*, 34, 145-155, 10.1139/t96-078, 1997.
- 835 Xie, C., Ni, P., Xu, M., Mei, G., and Zhao, Y.: Combined measure of geometry optimization and vegetation for expansive soil slopes,  
836 *Comput. Geotech.*, 123, 10.1016/j.compgeo.2020.103588, 2020.
- 837 Zhang, J., Luo, Y., Zhou, Z., Victor, C., and Duan, M.: Research on the rainfall-induced regional slope failures along the Yangtze  
838 River of Anhui, China, *Landslides*, 18, 1801-1821, 10.1007/s10346-021-01623-7, 2021a.



---

839 Zhang, J., Luo, Y., Zhou, Z., Chong, L., Victor, C., and Zhang, Y.: Effects of preferential flow induced by desiccation cracks on  
840 slope stability, *Eng. Geol.*, 288, 10.1016/j.enggeo.2021.106164, 2021b.  
841